

A dynamics-weighted principal components analysis of dominant atmospheric drivers of ocean variability with an application to the North Atlantic subpolar gyre

Daniel E. Amrhein¹, Dafydd Stephenson¹, and Luanne Thompson²

¹NSF National Center for Atmospheric Research

²University of Washington School of Oceanography

January 22, 2024

1 **A dynamics-weighted principal components analysis**
2 **of dominant atmospheric drivers of ocean variability**
3 **with an application to the North Atlantic subpolar gyre**

4 Daniel E. Amrhein^a Dafydd Stephenson^a LuAnne Thompson^b

5 ^a *NSF National Center for Atmospheric Research, Boulder, CO*

6 ^b *University of Washington School of Oceanography, Seattle, WA*

7 *Corresponding author:* Dan Amrhein, damrhein@ucar.edu

8 This work has been accepted to the Journal of Climate. The AMS does not guarantee that the copy
9 provided here is an accurate copy of the Version of Record (VoR).

10 ABSTRACT: This paper describes a framework for identifying dominant atmospheric drivers of
11 ocean variability. The method combines statistics of atmosphere-ocean fluxes with physics from
12 an ocean general circulation model to derive atmospheric patterns optimized to excite variability
13 in a specified ocean quantity of interest. We first derive the method as a weighted principal
14 components analysis and illustrate its capabilities in a toy problem. Next, we apply our analysis to
15 the problem of interannual upper ocean heat content (HC) variability in the North Atlantic Subpolar
16 Gyre (SPG) using the adjoint of the MITgcm and atmosphere-ocean fluxes from the ECCOv4-r4
17 state estimate. An unweighted principal components analysis reveals that North Atlantic heat and
18 momentum fluxes in ECCOv4-r4 have a range of spatiotemporal patterns. By contrast, dynamics-
19 weighted principal components analysis collapses the space of these patterns onto a small subset
20 – principally associated with the North Atlantic Oscillation – that dominates interannual SPG HC
21 variance. By perturbing the ECCOv4-r4 state estimate, we illustrate the pathways along which
22 variability propagates from the atmosphere to the ocean in a nonlinear ocean model. This technique
23 is applicable across a range of problems across Earth System components, including in the absence
24 of a model adjoint.

25 SIGNIFICANCE STATEMENT: While the oceans have absorbed 90% of the excess heat associ-
26 ated with human-forced climate change, the change in the ocean's heat content is not steady, with
27 peaks and troughs superimposed upon a general increase. These fluctuations come from chaotic
28 changes in the atmosphere and ocean, and can be hard to disentangle. We use this case of ocean heat
29 content variability to introduce a new method for determining the patterns of weather and climate
30 in the atmosphere that are most effective at generating fluctuations in the ocean. To do this, we
31 combine the statistics of recent atmospheric activity with output from a state-of-the-art numerical
32 ocean model that reveals physical processes driving changes in ocean quantities including ocean
33 heat content. This approach suggests that the atmospheric patterns that stimulate the most energetic
34 changes in ocean heat content in the northern North Atlantic are not the most energetic patterns
35 present in the atmosphere. We test our findings by preventing these patterns from affecting the
36 ocean in our numerical model, and measure a strong reduction in ocean heat content fluctuations.

37 **1. Introduction**

38 The ocean's distributions of momentum, thermal energy, salt, and other quantities evolve across
39 a range of length and time scales, reflecting contributions from solar radiation, turbulent fluxes of
40 heat and momentum at the air-sea interface, inputs from land and cryosphere, tides, hydrothermal
41 heating, and the internal variability of the turbulent ocean. Identifying processes and pathways
42 by which the ocean changes through time is important for revealing mechanisms and timescales
43 of predictability, fingerprints of anthropogenic changes, and the drivers of ocean variability and
44 change in the past and future. For many scales and processes, variability about an ocean mean
45 state may be usefully approximated as being driven by a stochastic atmosphere (Hasselmann
46 1976; Frankignoul and Hasselmann 1977; Kushnir et al. 2002), with secondary roles for ocean
47 turbulence, additional external drivers, and ocean-atmosphere feedbacks on time scales longer
48 than those associated with turbulent fluxes. Within these regimes, clarifying dominant pathways
49 of atmospheric influence on the ocean has the potential to provide parsimonious descriptions of
50 variability in a high-dimensional coupled system.

51 A traditional paradigm for exploring dominant drivers of ocean variability is to identify dynam-
52 ically important modes of variability in the atmosphere and then to evaluate their impact on the
53 ocean. In the North Atlantic, much of the atmospheric variability on seasonal and longer time

54 scales is associated with large-scale patterns in atmospheric circulation (Deser et al. 2010). In
55 particular, heat fluxes due to the North Atlantic Oscillation (NAO), the dominant mode of winter-
56 time atmospheric variability in the extratropical Northern Hemisphere (Hurrell and Deser 2009),
57 yield a characteristic “tripole” pattern with warmth in mid-latitudes and cooler temperatures in the
58 subpolar region and between the Equator and 30°N (Cayan 1992a,b; Marshall et al. 2001). The
59 NAO has been implicated in a range of ocean and climate variability. Frajka-Williams et al. (2017)
60 find that NAO-related surface heat fluxes likely explain a recent cooling in the subpolar North
61 Atlantic. Ortega et al. (2017) use an eddy permitting multi-century integration of a coupled model
62 to show that 62% of Labrador Sea density variance comes from low-frequency variations of the
63 NAO, with freshwater-driven ocean circulation changes having a larger effect at centennial time
64 scales. Bersch (2002) and Bersch et al. (2007) find that NAO wind anomalies are important for
65 Labrador Sea convection, northward heat transport through the SPG, and SPG structure, and Tesdal
66 et al. (2018) attribute recent freshening in the Labrador Sea to a spin-up in the SPG that may be
67 associated with NAO and Arctic Oscillation winds. Finally, Böning et al. (2006) and Lozier et al.
68 (2008) attribute decadal variations in SPG heat content (HC) and structure to combined influences
69 of NAO winds and buoyancy forcing.

70 However, there are also several lines of evidence that the NAO is not the only driver of hy-
71 drographic change in the SPG. Häkkinen et al. (2011) find that NAO-like patterns of wind stress
72 curl changes are not principally responsible for anomalous northward penetration of warm and
73 saline subtropical waters; instead, a secondary atmospheric circulation mode, resembling the East
74 Atlantic Pattern (EAP), was implicated that modulated NAO and storm track strength and that had
75 a larger projection onto SPG variability. Similarly, Barrier et al. (2014) performed forward sensi-
76 tivity analyses in a coupled model and found that different patterns of atmospheric variability were
77 associated with different time scales of ocean response. Kim et al. (2016) note that Labrador Sea
78 convection resumed in the winter of 2008/2009 after a hiatus beginning in the mid-1990s despite
79 that year having the same positive sign of NAO as the previous winter, and suggest a possible
80 connection to La Niña as an additional source of variability in deep Atlantic water masses.

81 While it is natural to evaluate the role of leading atmospheric modes in forcing ocean variability,
82 there is no requirement that a pattern derived to maximize the contribution to atmospheric variability
83 – for instance, through a regional atmospheric empirical orthogonal function / principal component

84 (EOF-PC; Lorenz (1956)) analysis or by regression of an index of atmospheric variables – will
85 be the dominant driver of variability for specified quantities in the ocean. A second, “bottom-up”
86 approach poses an inverse question: Given an ocean quantity of interest (hereafter QoI), such as
87 the heat content of an ocean volume, what is the hypothetical atmospheric variability that would
88 most efficiently excite it? This problem can be addressed using adjoint sensitivity analyses, which
89 leverage linearized ocean general circulation model dynamics to determine the origins of changes
90 in ocean QoIs. A growing body of literature uses adjoint sensitivities to study ocean hydrography
91 and dynamics (Marotzke et al. 1999; Köhl and Stammer 2004; Bugnion et al. 2006a,b; Czeschel
92 et al. 2010, 2012; Mazloff 2012; Fukumori et al. 2015; Pillar et al. 2016; Jones et al. 2018; Kostov
93 et al. 2019; Stephenson and Sévellec 2021a,b) revealing the adjoint approach as a powerful method
94 for determining pathways of change for ocean processes on climate-relevant scales.

95 A challenge in interpreting adjoint sensitivities is that their spatiotemporal structure is set by the
96 choice of the QoI and by the dynamics of the ocean model, with no information included about the
97 dynamics or statistics of the atmosphere except indirectly through their impact on simulated ocean
98 circulation. For instance, Stephenson and Sévellec (2021b) use an adjoint approach to show that
99 North Atlantic heat content variability can originate from winds along narrow bands that stimulate
100 Ekman transport and coastal upwelling. Similarly, Jones et al. (2018), following Marotzke et al.
101 (1999), decompose sensitivities of Labrador Sea HC into kinematic (constant circulation) and
102 dynamic (changing circulation) components and argue that HC changes can emerge advectively
103 from upstream source waters as well as via an ocean wave propagation mechanism excited from
104 forcing applied in a narrow band of the West African shelf. The narrow regions implicated by these
105 studies as optimal ocean drivers, with zonal length scales on the order of hundreds of kilometers,
106 reflect the scales of Rossby deformation radii in the ocean and ultimately of ocean model grid
107 boxes, in contrast to dominant length scales of wind variability of thousands of kilometers. A
108 consequence explored in previous literature both in the context of the El Niño-Southern Oscillation
109 (Kleeman and Moore 1997; Moore and Kleeman 1999; Zavala-Garay et al. 2003; Moore et al.
110 2006; Kleeman 2008) and the Atlantic circulation (Chhak and Moore 2007; Zanna and Tziperman
111 2008; Chhak et al. 2009) is that it is important to consider the projection of atmospheric variability
112 onto ocean sensitivities, rather than just the sensitivities themselves, in order to understand drivers
113 of ocean QoIs. A corollary is that the leading EOF of atmospheric variability need not be the most

114 important driver for the variability in a particular ocean diagnostic. Similarly, dominant patterns
115 (“stochastic optimals”, discussed further below) in ocean sensitivities to hypothetical atmospheric
116 conditions might not indicate important avenues by which the atmosphere drives ocean variability,
117 but might instead languish as “potential” pathways that are never actually activated.

118 This work combines “top-down” approaches informed by atmospheric statistics and “bottom-up”
119 approaches shaped by ocean dynamics through adjoint sensitivity analysis. As opposed to classical
120 EOF-PC analyses, we develop “empirical–dynamical functions” (EDFs) and “dynamics-weighted
121 principal components” (DPCs) that reflect both model dynamics and observed atmospheric statis-
122 tics. Our approach parallels model reduction procedures in control engineering, where one seeks
123 to reduce the degrees of freedom in a dynamical system (often to minimize computational burden)
124 while preserving features in both its “controllability” (i.e., where the system can go) and “observ-
125 ability” (any properties are of interest) of the system. Following work by Adamjan et al. (1971),
126 Moore (1981) describes an approach for “balanced truncation” that approximates a system in a
127 new basis informed by both controllability and observability. (See Antoulas (2005) and Brunton
128 and Kutz (2022) for additional introduction; Rowley (2005) shows that balanced truncation can be
129 computed efficiently using the singular value decomposition, which is the approach used here.) The
130 explicit connection to the present work is that atmospheric EOFs are an estimate of the principal
131 directions of controllability in the atmosphere, while stochastic optimals describe the principal
132 directions of observability in the case where we “observe” the atmosphere via its impact on the
133 ocean. Balanced truncation for model reduction has been applied previously in atmosphere-ocean
134 contexts by Farrell and Ioannou (2001), Moore et al. (2022), and Xu et al. (2024). Here, we focus
135 on dominant dynamical connections revealed by low-dimensional descriptions of forced ocean
136 variability.

137 The remainder of this paper is as follows. First, we present a derivation of the EDF–DPC approach
138 as an optimization problem. Under limiting conditions, EDFs recover EOFs and stochastic optimals.
139 Next, we demonstrate the approach in a simplified stochastic system and show how EDFs bear the
140 imprint of both sensitivities and forcing statistics. We then apply the EDF–DPC decomposition
141 using the adjoint of the MITgcm for the problem of understanding leading contributions by heat
142 fluxes and wind stress to interannual variability in North Atlantic Subpolar Gyre heat content. EDFs
143 outperform EOFs for driving variability in the linearized dynamical framework of the adjoint, and

144 the leading EDFs of both heat flux and wind stress are highly correlated with the NAO. To evaluate
 145 the efficacy of EDFs in a nonlinear model, we then rerun the ECCOv4-r4 ocean state estimate
 146 with atmospheric fluxes modified to omit EDFs. We find good correspondence between variance
 147 in the nonlinear MITgcm and what is predicted by linear (adjoint) dynamics, though in the case
 148 of heat fluxes, the removal of the leading NAO-like EDF pattern leads to a long-term cooling
 149 trend. Rerunning the ECCOv4-r4 state estimate with additional EDF perturbations illustrates the
 150 mechanisms by which atmospheric variability adjusts heat content in the North Atlantic.

151 **2. Theoretical Framework: Dynamically weighted principal components**

152 *a. Adjoint sensitivities and ocean variability*

153 As noted in Section 1, adjoint representations of ocean models are powerful tools for evaluating
 154 causes of ocean variability. We begin by introducing these concepts. We denote column vectors
 155 by bold variables and define the ocean model state vector, $\mathbf{x}(t)$, to be the set of prognostic variables
 156 (temperature, salinity, velocity, etc.) at time t at all latitudes, longitudes, and depths. Then the
 157 evolution of an ocean general circulation model can be written as

$$\mathbf{x}(t + \Delta t) = F[\mathbf{x}(t), \mathbf{u}(t)] \quad (1)$$

158 where F is a nonlinear operator and $\mathbf{u}(t)$ is a vector of time-varying atmospheric fluxes inclusive of
 159 all ocean model grid boxes and flux types. Next, we define a scalar, time-varying ocean “quantity
 160 of interest” $\text{QoI}(t)$ as a weighted sum over the model state vector,

$$\text{QoI}(t) = \sum_j \alpha^\top(t, t_j) \mathbf{x}(t_j), \quad (2)$$

161 where the vector $\alpha(t, t_j)$ consists of weights – reflecting, e.g., model grid box volumes and
 162 areal and temporal extent – defining the appropriate integral, for instance, to yield annually- and
 163 regionally-averaged heat content.

164 The adjoint sensitivity $\mathbf{s}(\tau)$ is given by

$$\mathbf{s}(\tau) = \frac{\partial \text{QoI}(t)}{\partial \mathbf{u}(t - \tau)}, \quad (3)$$

165 and is a linearized estimate of how $\text{QoI}(t)$ changes in response to small changes in \mathbf{u} at a time lead
 166 τ . Here and throughout this paper we make the simplifying stationarity assumption that $\mathbf{s}(\tau)$ is not
 167 a function of t . If a finite-amplitude change $\delta\mathbf{u}(\tau)$ is made in the fluxes (e.g., an increase in wind
 168 stress over the Northern Hemisphere), then the change $\delta\text{QoI}(t)$ is given by (modifying Fukumori
 169 et al. (2015))

$$\delta\text{QoI}(t) \approx \sum_{i=1}^{N_\tau} \mathbf{s}(\tau_i)^\top \delta\mathbf{u}(t - \tau_i), \quad (4)$$

170 where changes are summed over lags $\tau_1, \tau_2, \dots, \tau_{N_\tau}$ and we obtain equality when the model response
 171 to flux adjustments is linear. As described in greater detail in Section 4a, adjoint sensitivities are an
 172 output of the state estimation machinery underlying the ECCO state estimate, and can be produced
 173 from the MITgcm via automatic differentiation. They can be similarly computed from other models
 174 that have adjoint capabilities (the Regional Ocean Modeling System, ROMS, Moore et al. 2004; and
 175 Tangent and Adjoint Models for the Nucleus for European Modelling of the Ocean, NEMOTAM,
 176 Vidard et al. 2015).

177 We estimate total QoI variance σ_Σ^2 by assuming a linear response to fluxes and taking the
 178 expectation over time of squared QoI anomalies, $\sigma_\Sigma^2 = \langle (\delta\text{QoI}(t))^2 \rangle$. Substituting Eq. (4), we
 179 obtain

$$\sigma_\Sigma^2 = \sum_{i=1}^{N_\tau} \sum_{j=1}^{N_\tau} \mathbf{s}(\tau_i)^\top \langle \delta\mathbf{u}(t - \tau_i) \delta\mathbf{u}^\top(t - \tau_j) \rangle \mathbf{s}(\tau_j) \quad (5)$$

$$= \sum_{i=1}^{N_\tau} \sum_{j=1}^{N_\tau} \mathbf{s}(\tau_i)^\top \mathbf{C}_{ij} \mathbf{s}(\tau_j) \quad (6)$$

180 where \mathbf{C}_{ij} is the spatial covariance matrix of $\delta\mathbf{u}$ at time lag $\tau_i - \tau_j$. Covariances of air-sea fluxes can
 181 have complex structure in space and time, reflecting, e.g., the propagation of properties through
 182 the ocean and atmosphere. Here we discuss three approximations to make the description of this
 183 variability more tractable. First, we approximate \mathbf{C}_{ij} as separable in space and time (Hasselmann
 184 1993; Chen et al. 2021),

$$\mathbf{C}_{ij} = d_{ij} \mathbf{C}, \quad (7)$$

185 which assumes that covariances of atmospheric fluxes at different lags are the same, up to a lag-
 186 dependent scaling factor d_{ij}^2 . While there are limitations inherent in assuming separability – one

187 cannot, for instance, represent propagating waves – it nonetheless can describe fluxes with non-
 188 zero correlations in time (i.e., not just white noise) and non-stationary (time-evolving) covariances.
 189 Equation (6) can then be expressed in terms of a matrix trace as

$$\sigma_{\Sigma}^2 = \text{tr}(\mathbf{Z}\mathbf{C}) \quad (8)$$

190 where we define

$$\mathbf{Z} = \sum_{i=1}^{N_{\tau}} \sum_{j=1}^{N_{\tau}} d_{ij} \mathbf{s}(\tau_i) \mathbf{s}(\tau_j)^{\top}. \quad (9)$$

191 and we have followed Kleeman and Moore (1997) by incorporating information about flux non-
 192 stationarity and temporal covariance in \mathbf{Z} via the d_{ij} . This separability assumption underlies the
 193 dynamics-weighted principal components approach; the following two additional approximations
 194 can be convenient, but are not required. If a white noise assumption adequately represents space-
 195 time covariances, reflecting rapid decorrelation times of atmospheric fluxes relative to the ocean
 196 circulation (Hasselmann 1976; Frankignoul and Hasselmann 1977), then one can set lag flux cor-
 197 relations to zero by choosing $d_{ij} = \delta_{ij} d_{ij}$ where δ_{ij} is the Kronecker delta. Note that this form still
 198 represents changes in the variance of fluxes through time, which can be large over a seasonal cycle.
 199 Finally, if fluxes are furthermore assumed to be stationary (constant spatial covariance through
 200 time), then $d_{ij} = \delta_{ij}$ and $\mathbf{Z} = \mathbf{S}\mathbf{S}^{\top}$, where the matrix

$$\mathbf{S} = [\mathbf{s}(\tau_1), \mathbf{s}(\tau_2), \dots, \mathbf{s}(\tau_{N_{\tau}})] \quad (10)$$

201 is formed by concatenating sensitivities across N_{τ} discrete lags. The model stochastic optimals
 202 (Farrell and Ioannou 1996; Kleeman and Moore 1997) are the left singular vectors of \mathbf{S} .

203 *b. Optimal atmospheric drivers of ocean variability*

204 Next, our goal is to decompose atmospheric variability into patterns and corresponding time
 205 series, analogous to EOF–PC analysis. We do this by combining adjoint sensitivities from an
 206 ocean model and atmospheric fluxes to define a matrix the square of whose diagonal elements sum
 207 to the QoI variance. The singular vectors of that matrix yield a set of flux patterns ordered by their

208 contributions to ocean variability. Begin by defining a data matrix

$$\mathbf{U} = (N_t - 1)^{-\frac{1}{2}} [\mathbf{u}(t_0), \mathbf{u}(t_1), \dots, \mathbf{u}(t_{N_t})] \quad (11)$$

209 consisting of vectors $\mathbf{u}(t_i)$ of fluxes concatenated column-wise across N_t discrete times. We have
 210 scaled \mathbf{U} so that the zero-lag flux covariance can be estimated as

$$\mathbf{C} = \mathbf{U}\mathbf{U}^\top \quad (12)$$

211 and flux PCs and EOFs are the left and right singular vectors of \mathbf{U} , respectively. We express our
 212 decomposition as

$$\mathbf{U} = \sum_{k=1}^{N_{DPC}} \mathbf{p}_k \mathbf{t}_k^\top \quad (13)$$

213 where \mathbf{p}_k denotes the k^{th} “empirical–dynamical function” (EDF) and \mathbf{t}_k the corresponding
 214 “dynamics-weighted principal component” (DPC) up to an integer N_{DPC} . For notational con-
 215 venience we stipulate that $\|\mathbf{t}_k\| = 1$, where $\|\cdot\|$ denotes the vector l^2 norm, so that $\|\mathbf{p}_k\|^2$ is the flux
 216 variance accounted for by the k^{th} EDF-DPC pair in \mathbf{U} . We require that EDFs represent distinct
 217 processes insofar as their variability is uncorrelated in time within \mathbf{U} , meaning that (like PCs) the
 218 \mathbf{t}_k are orthonormal; however, unlike EOFs, the EDFs are not generally orthogonal in space. Right
 219 multiplying (13) by \mathbf{t}_k and using orthonormality, we find that the \mathbf{p}_k are given by the projection of
 220 \mathbf{t}_k onto \mathbf{U} ,

$$\mathbf{U}\mathbf{t}_k = \mathbf{p}_k. \quad (14)$$

221 To find the set of EDF–DPC pairs, we solve an optimization problem. We first substitute (13)
 222 into (8) to obtain

$$\sigma_\Sigma^2 = \text{tr} \left(\sum_{i=1}^{N_{DPC}} \sum_{j=1}^{N_{DPC}} \mathbf{Z} \mathbf{p}_i \mathbf{t}_i^\top \mathbf{t}_j \mathbf{p}_j^\top \right). \quad (15)$$

223 By orthonormality of the \mathbf{t}_k and Eq. (14) we find

$$\sigma_{\Sigma}^2 = \sum_{k=1}^{N_{DPC}} \text{tr}(\mathbf{Z}\mathbf{p}_k\mathbf{p}_k^{\top}) \quad (16)$$

$$= \sum_{k=1}^{N_{DPC}} \|\mathbf{Z}^{\frac{\top}{2}}\mathbf{U}\mathbf{t}_k\|^2. \quad (17)$$

224 where we have defined a matrix decomposition $\mathbf{Z} = \mathbf{Z}^{\frac{1}{2}}\mathbf{Z}^{\frac{\top}{2}}$ and used the invariance of trace under
 225 cyclic permutations. We can now define an optimization problem to find the leading DPC \mathbf{t}_1 that
 226 maximizes the contribution to QoI variance $\sigma_1^2 = \|\mathbf{Z}^{\frac{\top}{2}}\mathbf{U}\mathbf{t}_1\|^2$,

$$\mathbf{t}_1 = \underset{\mathbf{t}}{\text{argmax}} \|\mathbf{Z}^{\frac{\top}{2}}\mathbf{U}\mathbf{t}\|^2. \quad (18)$$

227 The solution to (18) for $\|\mathbf{t}_1\| = 1$ is given by the leading right singular vector of the matrix $\mathbf{Z}^{\frac{\top}{2}}\mathbf{U}$.
 228 Generalizing beyond the leading DPC, if we define the singular vector decomposition as

$$\mathbf{Z}^{\frac{\top}{2}}\mathbf{U} = \mathbf{L}\mathbf{\Sigma}\mathbf{T}^{\top} = \sum_{k=1}^{N_{DPC}} \mathbf{l}_k\sigma_k\mathbf{t}_k^{\top}, \quad (19)$$

229 then the full set of DPCs is given by the columns \mathbf{t}_k of \mathbf{T} . DPCs are ordered by their con-
 230 tributions, σ_k^2 , to the total QoI variance. The number of meaningful EDF–DPC pairs N_{DPC}
 231 is given by the the number of nonzero σ_k , i.e., the rank of the matrix $\mathbf{Z}^{\frac{\top}{2}}\mathbf{U}$, and obeys
 232 $N_{DPC} \leq \min(\text{rank}(\mathbf{Z}^{\frac{\top}{2}}), \text{rank}(\mathbf{U}))$.

233 EDFs recover familiar results in limiting cases. First, the case where \mathbf{C} is proportional to the
 234 identity matrix corresponds to fluxes that are Gaussian white noise in space. If the fluxes are also
 235 stationary Gaussian white noise in time, then EDFs are equivalent to the stochastic optimals of
 236 the model. Similarly, if \mathbf{Z} is proportional to the identity matrix, then the model is insensitive to
 237 spatial patterns in fluxes, and the EDFs are equivalent to the flux EOFs. At the opposite limit of
 238 spatial degrees of freedom, when fluxes are proportional to a single spatial pattern at all times, the
 239 (single) EDF is simply that pattern. When adjoint sensitivities are proportional to a single spatial
 240 pattern \mathbf{s}_1 at all lags, then $\mathbf{t}_1 = \mathbf{U}^{\top}\mathbf{s}_1/(\mathbf{s}_1^{\top}\mathbf{C}\mathbf{s}_1)$ and the single EDF is proportional to the product of
 241 the spatial covariance with \mathbf{s}_1 , $\mathbf{p}_1 = \mathbf{C}\mathbf{s}_1(\mathbf{s}_1^{\top}\mathbf{C}\mathbf{s}_1)$.

242 Finally, we can construct “impact maps” indicating where QoI variance originates in space for
 243 each EDF. As noted by Stephenson and Sévellec (2021b), the map of total variance contributed by
 244 fluxes is given by

$$\mathbf{v}_\Sigma = \text{diag}(\mathbf{Z}\mathbf{C}) \quad (20)$$

245 where $\text{diag}(\mathbf{A})$ denotes the vector lying along the diagonal of a matrix \mathbf{A} . Substituting Eq. (19),
 246 we obtain

$$\mathbf{v}_\Sigma = \sum_{k=1}^{N_{DPC}} \text{diag}\left(\mathbf{Z}^{\frac{1}{2}}\mathbf{l}_k\sigma_k\mathbf{t}_k^T\mathbf{U}^T\right) \quad (21)$$

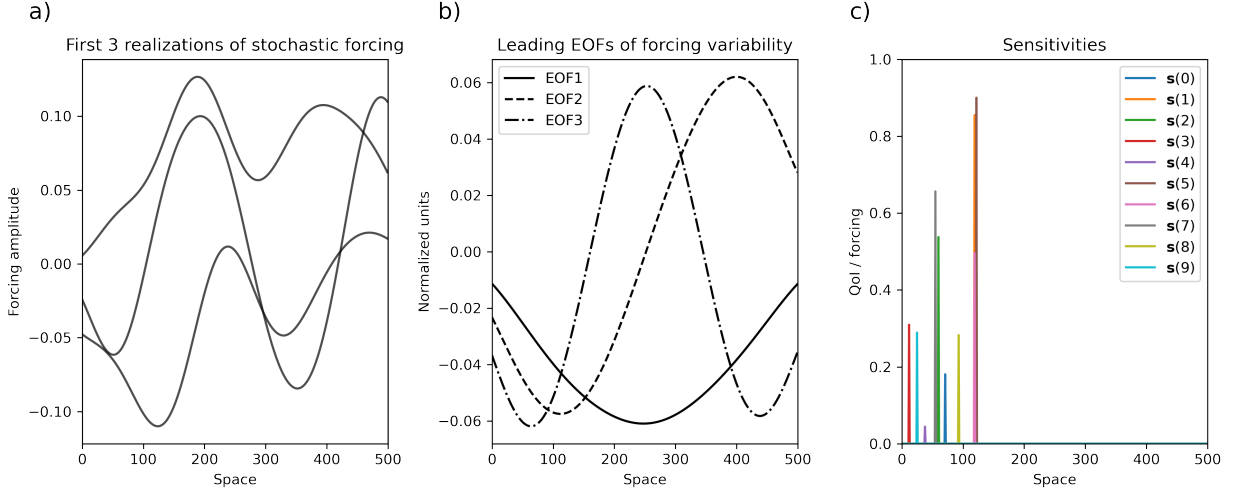
247 from which we can write the map of variance contributions for the k^{th} EDF-DPC pair as

$$\mathbf{v}_k = \sigma_k\left(\mathbf{Z}^{\frac{1}{2}}\mathbf{l}_k\right) \odot \mathbf{p}_k, \quad (22)$$

248 where \odot denotes the element-wise product. As we will show in Section 4, impact maps are are
 249 useful for diagnosing dominant pathways of variance to the QoI.

250 3. Demonstration in a simple stochastic system

255 Before applying the EDF method in the context of a full ocean GCM, we illustrate it in an
 256 idealized one-dimensional configuration (Figure 1). In this setup, we generate realizations of
 257 random fluxes that are correlated in space (mimicking large-scale atmospheric variability) and
 258 stationary Gaussian white noise in time (consistent with Hasselmann (1976)). Three realizations
 259 of this stochastic process are shown in Figure 1a. The leading EOFs computed from 10,000
 260 realizations of these fluxes (Figure 1b) have length scales comparable to the extent of the domain and
 261 are approximately symmetric about its midpoint. Next, we generate sensitivities of a hypothetical
 262 QoI to fluxes at 10 lags as scaled delta functions in the leftmost third of the domain (Figure 1c) with
 263 randomly chosen scalings. These sensitivities mimic properties of adjoint sensitivities computed
 264 in ocean models, which often have shorter length scales than those in the atmospheric variability
 265 and are concentrated within a subset of the spatial domain, as described in Section 1. In the case
 266 shown where sensitivities across different lags have nonzero values at distinct spatial locations,



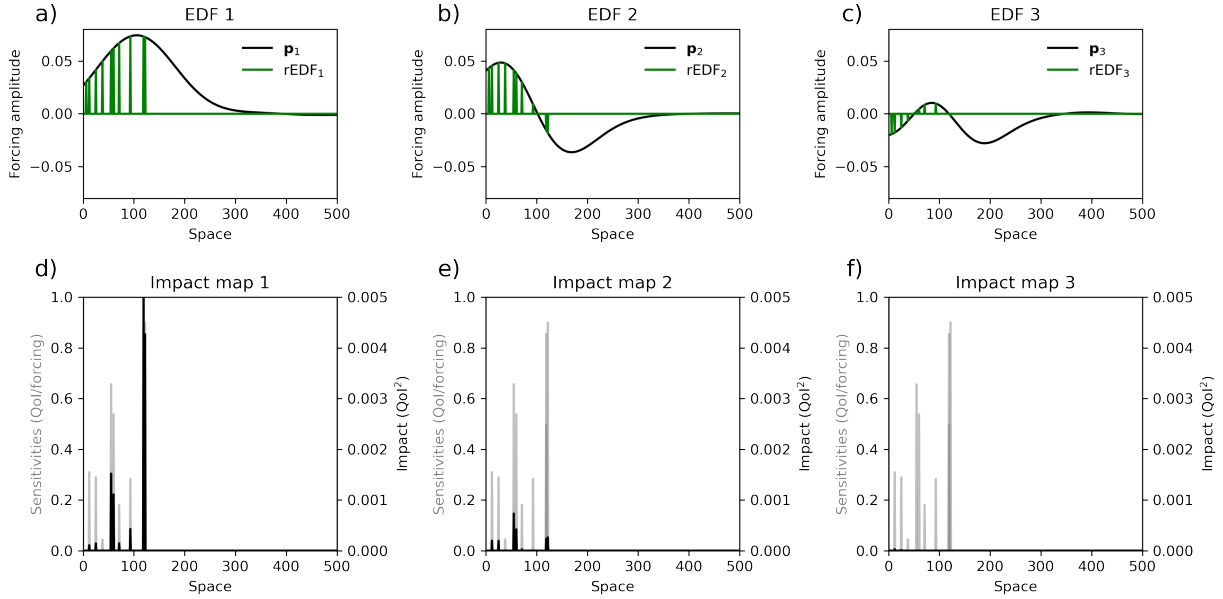
251 FIG. 1. Setup for EDF–DPC analysis in a simple stochastic system. a) Stochastic forcing in a synthetic one-
 252 dimensional system is generated by smoothing Gaussian white noise in space. b) Leading EOFs of this forcing
 253 have large spatial scales and are approximately symmetric in space. c) Adjoint sensitivities $\mathbf{s}(\tau)$ are randomly
 254 generated with different values across ten time lags.

267 the stochastic optimals (computed as the left singular vectors of \mathbf{S} , not shown) are simply delta
 268 functions at those locations, ordered by their magnitudes.

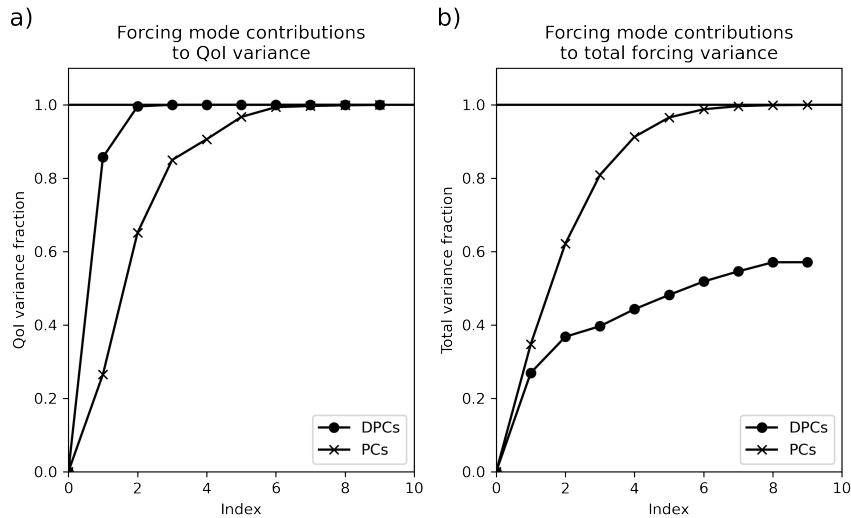
274 To compute DPCs, we construct \mathbf{U} from Eq. (11) using 10,000 realizations of stochastic forcing
 275 and \mathbf{S} from Eq. (10), concatenating across the ten lags. In the stationary white noise case, $\mathbf{Z} = \mathbf{S}\mathbf{S}^\top$
 276 (Section 2a) and we can use $\mathbf{Z}^{\frac{1}{2}} = \mathbf{S}$. Then computing singular vectors of $\mathbf{S}^\top\mathbf{U}$ (Eq. (19)) and
 277 EDFs (Eq. (14)) yields ten EDF-DPC pairs with nonzero contributions summing to the total QoI
 278 variance. In contrast to the leading EOFs, leading EDF patterns (Figure 2a-c) are asymmetric in
 279 space, reflecting the preference imparted by the adjoint sensitivities for the left side of the domain.
 280 While the EDF patterns are not orthogonal in space, the corresponding DPC time series (not
 281 shown) are orthonormal white noise.

284 Each EDF–DPC pair’s contribution to QoI variance is given by the corresponding squared
 285 singular value of $\mathbf{S}^\top\mathbf{U}$ (Figure 3a, circles). For comparison, the QoI variance contribution from
 286 the i^{th} EOF \mathbf{e}_i is given by

$$\left(\sigma_i^{\text{EOF}}\right)^2 = \|\lambda_i \mathbf{S}^\top \mathbf{e}_i\|^2 \quad (23)$$



269 FIG. 2. a-c) The leading three EDFs (spatial patterns) computed in a simple 1-D example. “Reduced” EDFs
 270 ($rEDF_k$, green lines) show the subset of each EDF that contributes to QoI variability; other nonzero EDF
 271 values arise from spatial forcing covariances. d-f) Impact maps (Equation 22) illustrating contributions to QoI
 272 variance across space (black lines) for each EDF. For comparison, these are overlaid on the distribution of adjoint
 273 sensitivities across lags (gray lines, also shown in Figure 1c).



282 FIG. 3. Comparison of contributions from EDF-DPC and EOF-PC pairs to a) QoI variance and b) total forcing
 283 variance in a simple 1-D example.

287 where λ_i^2 is the contribution of the i^{th} EOF to the total flux variance. As expected, leading
288 DPCs account for a greater fraction of QoI variance than do leading EOFs, with a more rapid
289 convergence of cumulative variance explained (compare circles and X's in Figure 3a). We can
290 perform the equivalent comparison for contributions to the total flux variance by comparing the λ_i^2
291 to $\|\mathbf{p}_k\|^2$, where the latter describes how much of the variance in \mathbf{U} is explained by the k^{th} EDF-
292 DPC pair, revealing that EOFs maximize contributions to total flux variability more effectively
293 than DPCs (Figure 3b). Thus, EDF-DPC pairs can have an outsize impact on variability in the QoI
294 relative to their contribution to flux variability.

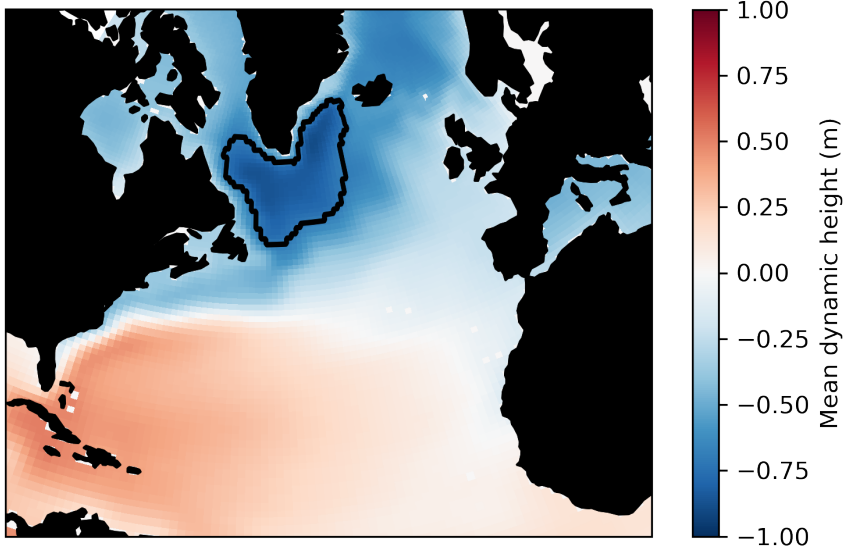
295 Impact maps (black lines, Figure 2 d-f) are computed using Eq. (22) and indicate the amount of
296 QoI variance contributed by each EDF as a function of space, which is determined by a combination
297 of local sensitivity and EDF amplitudes. By ranking the impact map and selecting locations with
298 leading impacts, we can define a “reduced” EDF (rEDF), plotted in green in Figure 2 (a-c). As we
299 discuss in the next section, the rEDF is useful for clarifying the dominant mechanisms by which
300 the EDF impacts QoI variance. In this simplified case, all of the QoI variance is explained by the
301 subset of locations with nonzero sensitivities. At other locations, EDFs are nonzero because of
302 spatial correlations in the fluxes, and have no impact on the QoI.

303 **4. Leading atmospheric drivers of interannual Subpolar Gyre heat content variability**

304 Next, we examine the EDFs of upper-ocean heat content in the North Atlantic Subpolar Gyre
305 (SPG). This region was chosen for its dynamical importance for AMOC strength across models
306 (Yeager et al. 2021; Oldenburg et al. 2021) including the MITgcm (Kostov et al. 2022) as well as for
307 being a place where ocean dynamics are thought to play an important role in sea surface temperature
308 variability (Buckley et al. 2014, 2015; Wills et al. 2019). This work follows previous studies using
309 the adjoint for investigations of drivers of SPG variability (Jones et al. 2018; Stephenson and
310 Sévellec 2021b).

314 *a. Model setup*

315 The MITgcm (Marshall et al. 1997; Adcroft et al. 2004) simulates ocean circulation under
316 hydrostatic and Boussinesq assumptions. Here we use the nominal 1 degree configuration with 50
317 vertical levels used for the ECCO version 4, release 4 (ECCOv4-r4) state estimate (Wunsch and



311 FIG. 4. Definition of the region of interest used for adjoint sensitivities. The black outline demarcates the
 312 North Atlantic Subpolar Gyre region, chosen as the largest negative closed contour of time mean dynamic height
 313 in the ECCOv4-r4 state estimate (-70 cm) following Foukal and Lozier (2017).

318 Heimbach 2007; Forget et al. 2015b; Fukumori et al. 2018) with two sets of initial and boundary
 319 conditions: one to construct the flux data matrix \mathbf{U} , and the other to construct adjoint sensitivities.
 320 We construct \mathbf{U} per Equation (11) from fluxes derived for ECCOv4-r4, which assimilates a range
 321 of observations to produce a dynamically consistent history of recent ocean variability spanning
 322 1992 to 2017. We construct \mathbf{U} separately for ECCOv4-r4 heat fluxes and wind stress at 6 hourly
 323 resolution, concatenating zonal and meridional wind stress into a single matrix. The statistics of
 324 ECCOv4-r4 air-sea fluxes include effects from adjustments of the forcing, initial conditions and
 325 mixing parameterizations made to create a product that fits ocean observations; we make no effort
 326 to separate this contribution and neglect any possible erroneous impact to large-scale patterns of
 327 flux covariance.

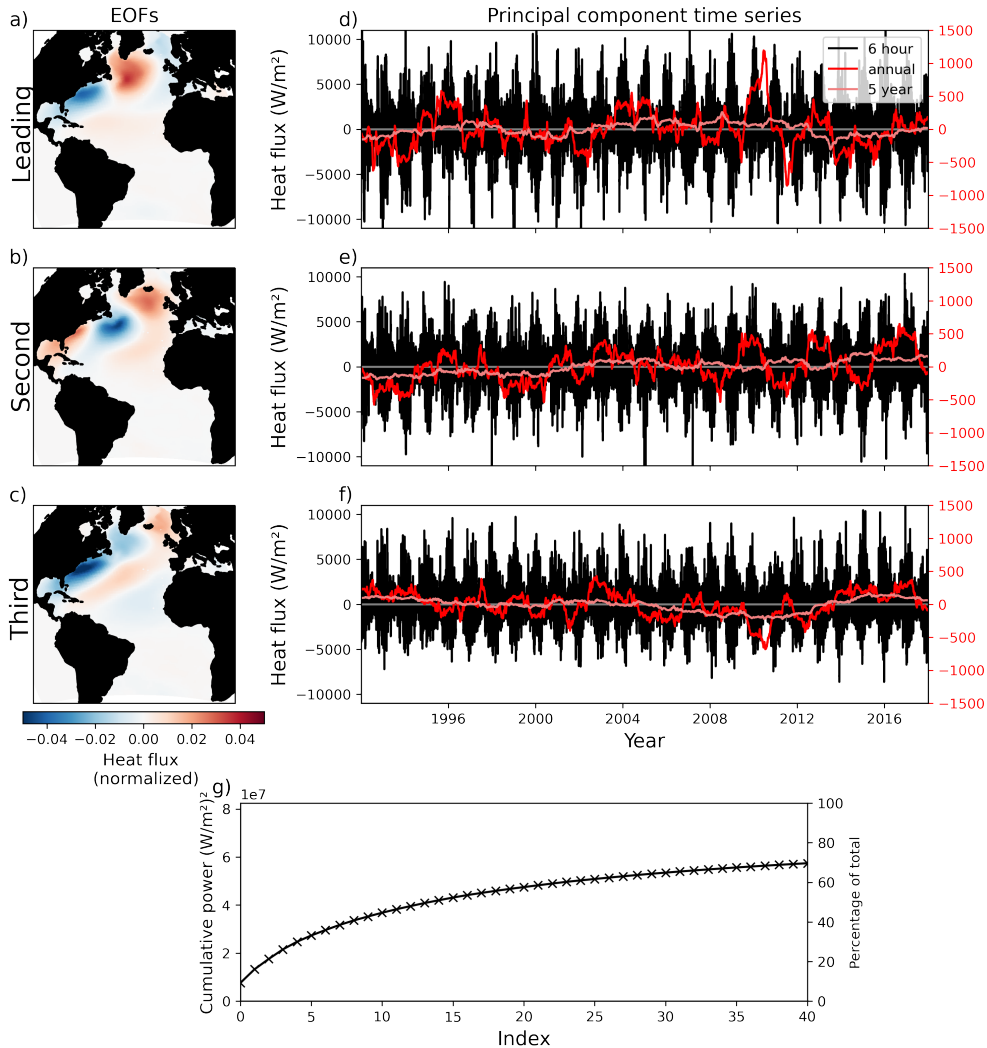
328 The second set of initial and boundary conditions are used to construct the ocean state about
 329 which the adjoint is computed. Here we use the initial conditions and forcing of Wolfe et al. (2017),
 330 who spun up the MITgcm for 5400 years under CORE Normal Year Forcing (Large and Yeager
 331 2004). Using an annually repeating forcing set for the adjoint ensures that ocean dynamics are not
 332 subject to forced interannual variability, such that any variability diagnosed with our method can

333 be attributed to historical fluctuations in U over the ECCOv4-r4 period. Following Foukal and
334 Lozier (2017), we define the SPG as the area enclosed by the largest negative closed contour (-70
335 cm) of dynamic height anomaly in the climatology of the ECCOv4-r4 state estimate (Figure 4).
336 Note that this approach yields an SPG definition with a reduced footprint in the eastern part of the
337 basin relative to Foukal and Lozier (2017) (cf. their Figure 3a). We compute the model adjoint
338 using TAF (Transformation of Algorithms in Fortran; Giering and Kaminski 1998) and compute
339 sensitivities of annual mean heat content (HC) above 700m in the SPG to heat fluxes (HF) and
340 zonal and meridional wind stress (WS) in an Atlantic domain from 35° S to 80° N at lags from 0
341 hours to 40 years.

348 *b. Atmospheric fluxes and sensitivities in the ECCOv4-r4 state estimate and the MITgcm*

349 Heat flux and wind stress variability in ECCOv4-r4 is summarized by EOF-PC analysis (Figures
350 5 and 6). In all cases, because we are focused on interannual variability in SPG HC, we compute
351 fluxes as anomalies about a seasonal cycle estimated from the ECCOv4-r4 climatology. The
352 spectrum of squared singular values in the EOF-PC analyses of HF and WS both show a gradual
353 convergence to the total power (the sum of squared singular values; Figures 5g and 6g), indicating
354 that fluxes are composed of a diversity of patterns of roughly equal importance. Leading EOFs of
355 HF (Figure 5 a-c) extend across the North Atlantic, with centers of action reflecting gyre structure
356 and the path of the Gulf Stream. By contrast, leading EOFs of WS (Figure 6 a-c) are centered
357 primarily over the SPG, with only small-amplitude correlated structures in the rest of the domain.
358 Principal components for both HF and WS (Figures 5 and 6, d-f) have variability across a range
359 of timescales, as demonstrated by the low frequency variability of running means computed over
360 annual and 5-year intervals. While we have subtracted the climatological seasonal cycle, the 6-
361 hourly product shows a strong annual cycle in the variance of WS and particularly HF, consistent
362 with a North Atlantic that is stormier and more variable in winter.

368 Leading stochastic optimals (SOs) and their corresponding lag time series illustrate potential
369 pathways for surface fluxes to change SPG HC in the MITgcm (Figures 7 and 8). We compute
370 SOs and accompanying lag time series as left and right singular vectors of S , which is constructed
371 by concatenating snapshots of sensitivities at lag increments of five days spanning 0 to 40 years
372 (Equation (10)). The leading SOs capture large fractions of the spatiotemporal variability in



342 FIG. 5. EOFs (leading spatial patterns; a-c) and PCs (corresponding time series, d-f, shown at 6-hourly
 343 resolution and with annual and 5-year moving averages applied), for heat flux anomalies about annual climatology
 344 in the ECCOv4-r4 state estimate. Spatial patterns are reported in normalized units. While the estimated seasonal
 345 cycle has been removed from heat fluxes, there is a prominent seasonal cycle in the amplitude of variability in
 346 all three principal components. g) Variance accounted for by EOF-PC pairs converges gradually to the total
 347 variance.

373 adjoint sensitivities across lags, with the leading SO accounting for roughly 70% and 50% of
 374 the structure in the HF and WS cases, respectively (Figures 7g and 8g). HF perturbations that
 375 are mostly restricted to the SPG (Figure 7a) lead to HC anomalies that persist for several years,
 376 with a strong dependence on the season when the perturbation is applied (Figure 7d). In contrast,

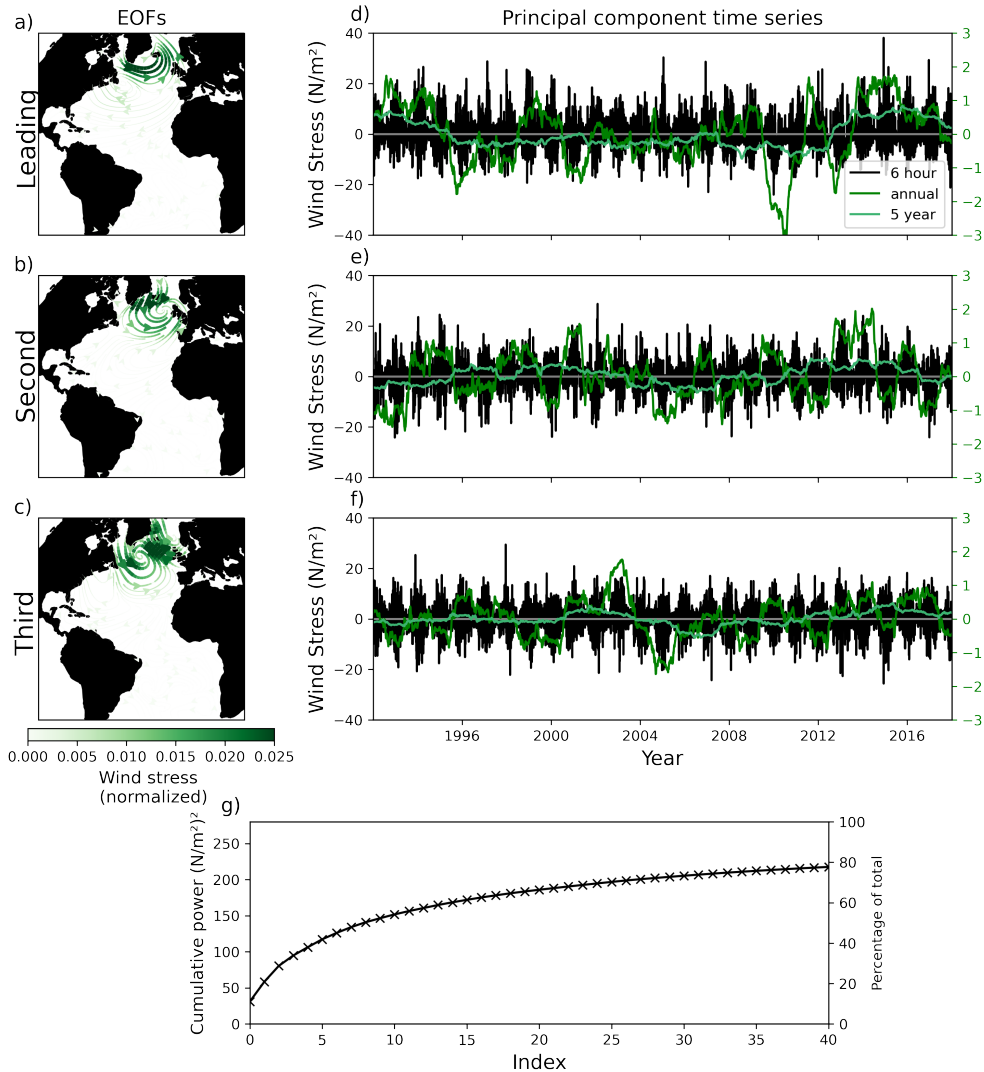
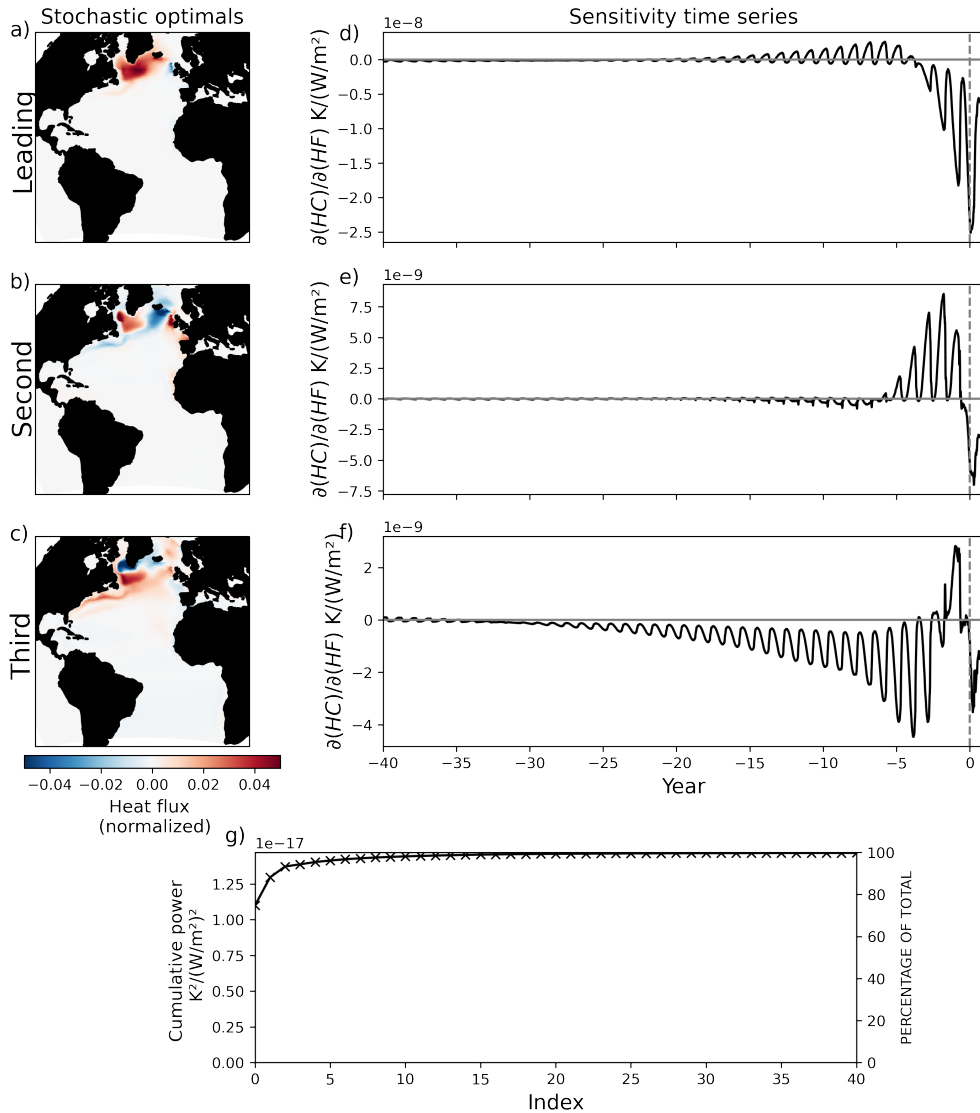


FIG. 6. Same as Figure 5 but for wind stress.

377 HF perturbations with anomalies extending along the model Gulf Stream (Figure 7c) persist over
 378 decadal timescales, again with strong seasonal dependence (Figure 7f). The leading HF SO (Figure
 379 7a) strongly resembles the regional QoI definition in the SPG (cf. 4) and reflects local heating, with
 380 modest additional contributions from heat fluxes upstream in the Gulf Stream. The leading WS
 381 SO (Figure 8a) is a combination of local effects within the SPG and coastal upwelling mechanisms
 382 described by Jones et al. (2018) and Stephenson and Sévellec (2021b), whereby anomalies in HC
 383 propagate as Kelvin waves counterclockwise around the North Atlantic towards the Labrador Sea.
 384 While both HF and WS sensitivities have a seasonal dependence, it is stronger for HF, with NH
 385 wintertime fluxes having up to an order of magnitude greater impact in subsequent years than



363 FIG. 7. Stochastic optimals (a-c) and corresponding lag time series (d-f) illustrating the hypothetical most
 364 efficient patterns of heat fluxes for driving SPG HC variability. Dotted lines at the zero-lag mark denote the
 365 beginning of the one-year period over which SPG HC is averaged to compute the QoI. Cumulative power (g)
 366 indicates that roughly 90% of the structure of adjoint sensitivities is accounted for by the leading three SO-lag
 367 pairs.

386 summertime fluxes. This seasonal dependence is consistent with a contrast between a strong,
 387 shallow model pycnocline in the summer relative to deeper winter mixed layers that allow greater
 388 penetration of thermal anomalies (Stommel 1979; MacGilchrist et al. 2021).

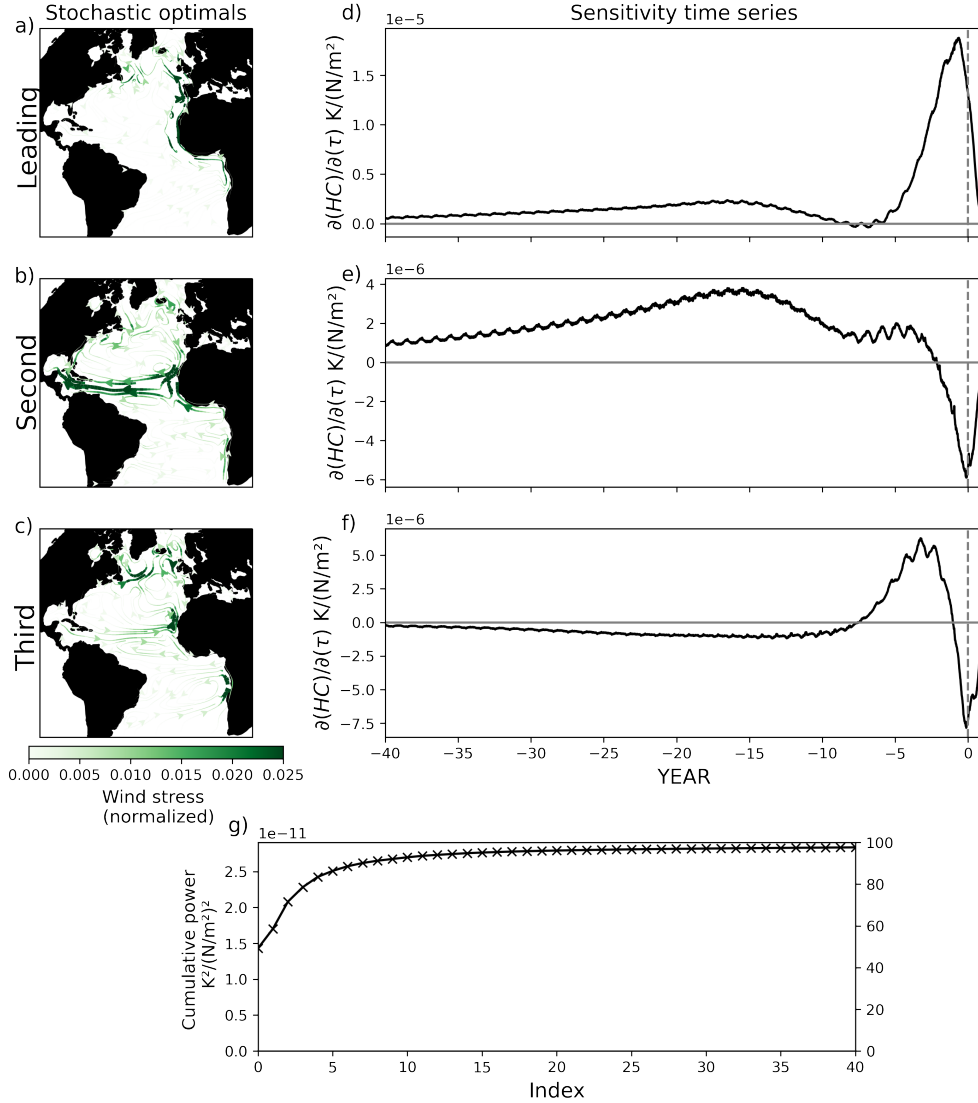
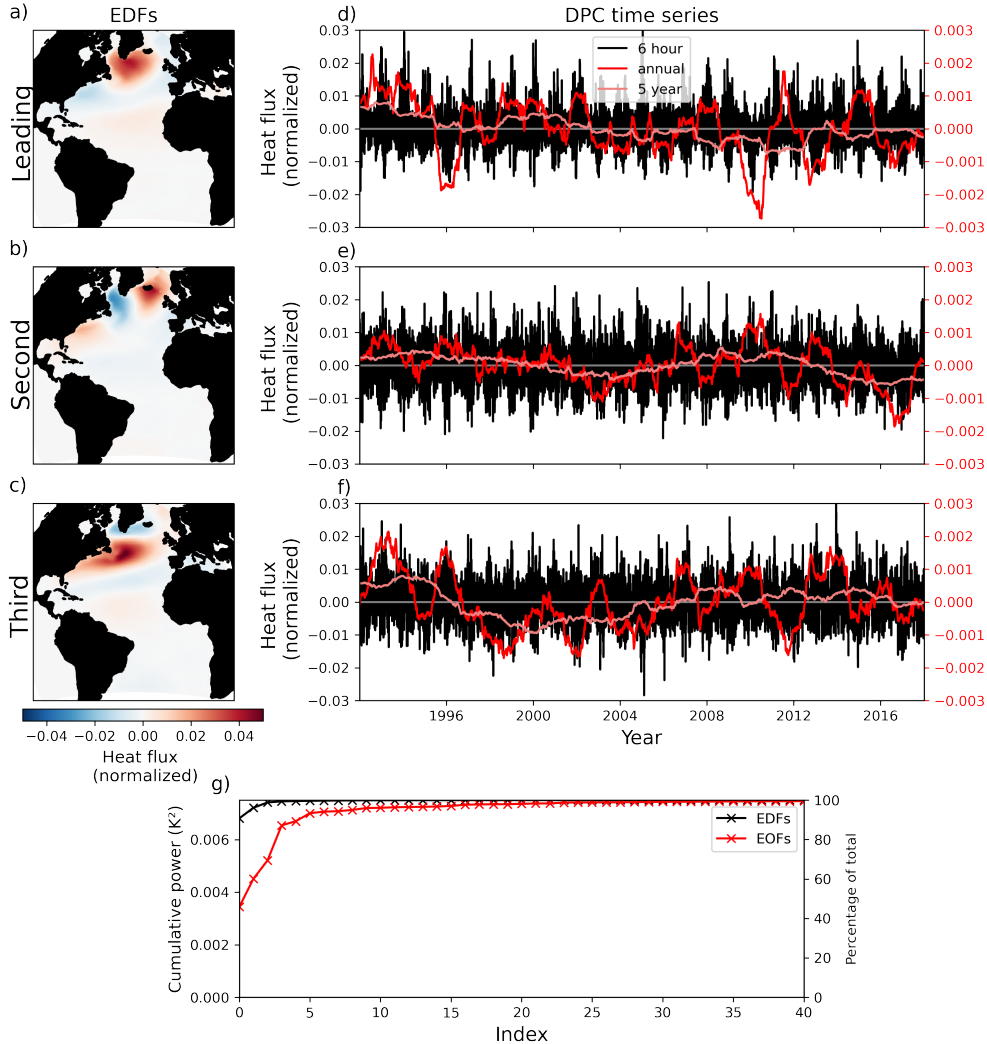


FIG. 8. Same as Figure 7, but for wind stress.

389 *c. Dominant atmospheric drivers of Subpolar Gyre heat content variability*

396 The EOFs (Figures 5 a-c and 6 a-c) and SOs (Figures 7 a-c and 8 a-c) for SPG HC illustrate
 397 the dichotomy discussed in Section 1: EOFs are generally large scale and agnostic of the ocean
 398 QoI, while SOs specifically reflect SPG properties defined by the QoI, with shorter length scales.
 399 Next we compute EDF–DPC pairs to reconcile these perspectives. The typical autocorrelation
 400 structure of flux principal components is roughly 1.5 days (not shown), substantially shorter than
 401 the interannual time scales of interest, so we compute \mathbf{Z} following (9), consistent with a white



390 FIG. 9. Pairs of empirical-dynamical functions (a-c) and corresponding dynamics-weighted principal com-
 391 ponents (d-f) illustrate the statistically most efficient subset of heat fluxes in the ECCOV4-r4 state estimate for
 392 driving SPG HC variability in the MITgcm. Both EDFs and DPCs are plotted in normalized units; red DPC
 393 curves indicate moving averages of 1 and 5 years. Panel g) compares QoI variance accounted for by leading
 394 EDF-DPC (black) and EOF-PC (red) pairs; the leading EDF-DPC pair is expected to account for roughly 90%
 395 of the interannual variability in SPG HC caused by HF roughly double that explained by the leading EOF.

402 noise assumption. We estimate seasonal nonstationarity in variance amplitudes (to specify the d_i
 403 in (9)) following Stephenson and Sévellec (2021a) (not shown).

404 The leading EDF-DPC pairs of HF and WS account for a high fraction of the SPG HC variability
 405 driven by those fluxes (black lines in Figures 9g and 10g; note that the total power reported in

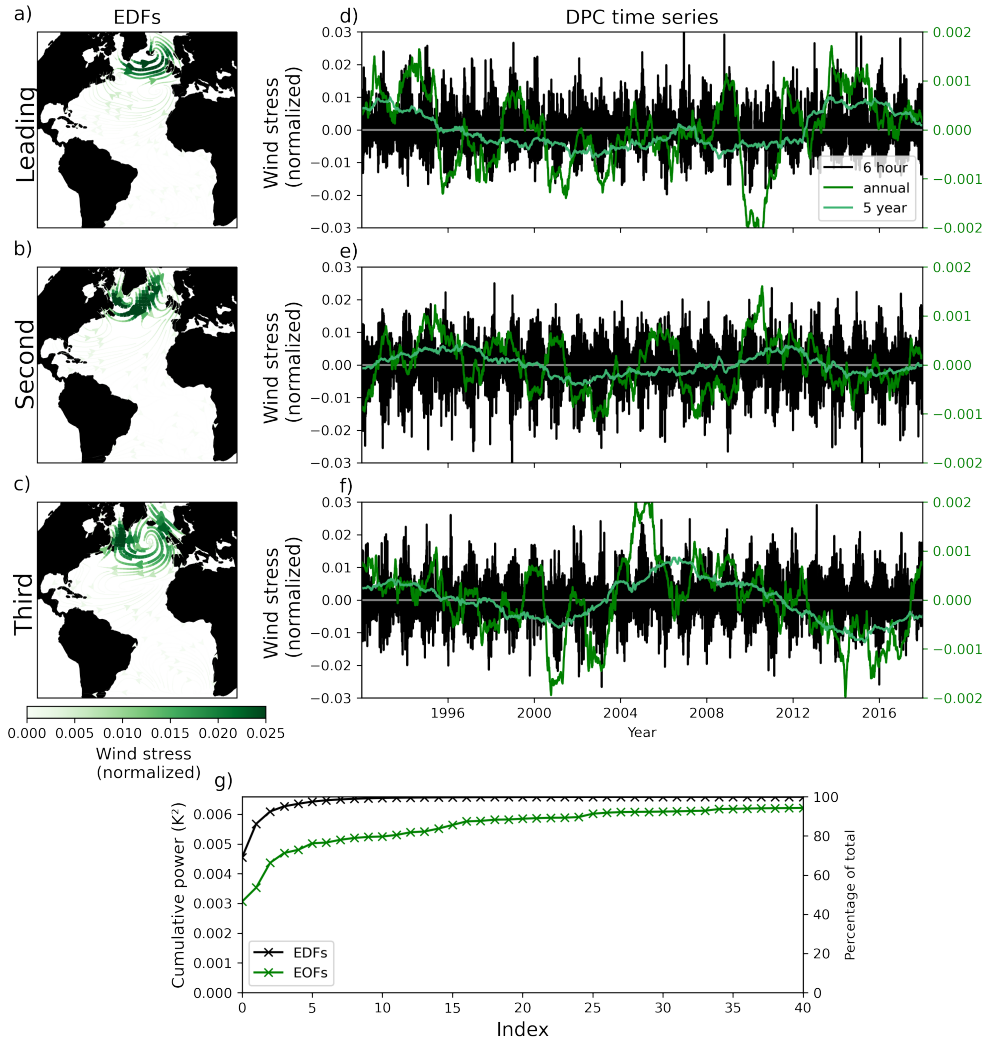


FIG. 10. Same as Figure 9 but for wind stress.

406 these figures is the total power contributed individually by HF and WS to the QoI). As expected,
 407 contributions to QoI variance from leading EDFs are larger than for EOFs (green and red lines
 408 in Figures 9g and 10g; cf. simple model results in Figure 3a). The leading HF EDF (Figure
 409 9a) consists primarily of a single center of action centered on the SPG with secondary zonal
 410 bands to the south, distinct from the leading EOF (Figure 5a), which has a stronger heat flux
 411 minimum over the model Gulf Stream. By contrast, the leading EDF of wind stress (Figure 10a)
 412 qualitatively resembles the leading WS EOF (Figure 6a). Similar to PCs, DPCs (Figures 9 d-f and
 413 10 d-f) are approximately white noise in time, with a typical maximum autocorrelation timescale
 414 of approximately 1.5 days. The seasonal cycle of variance is less pronounced in HF DPCs than in

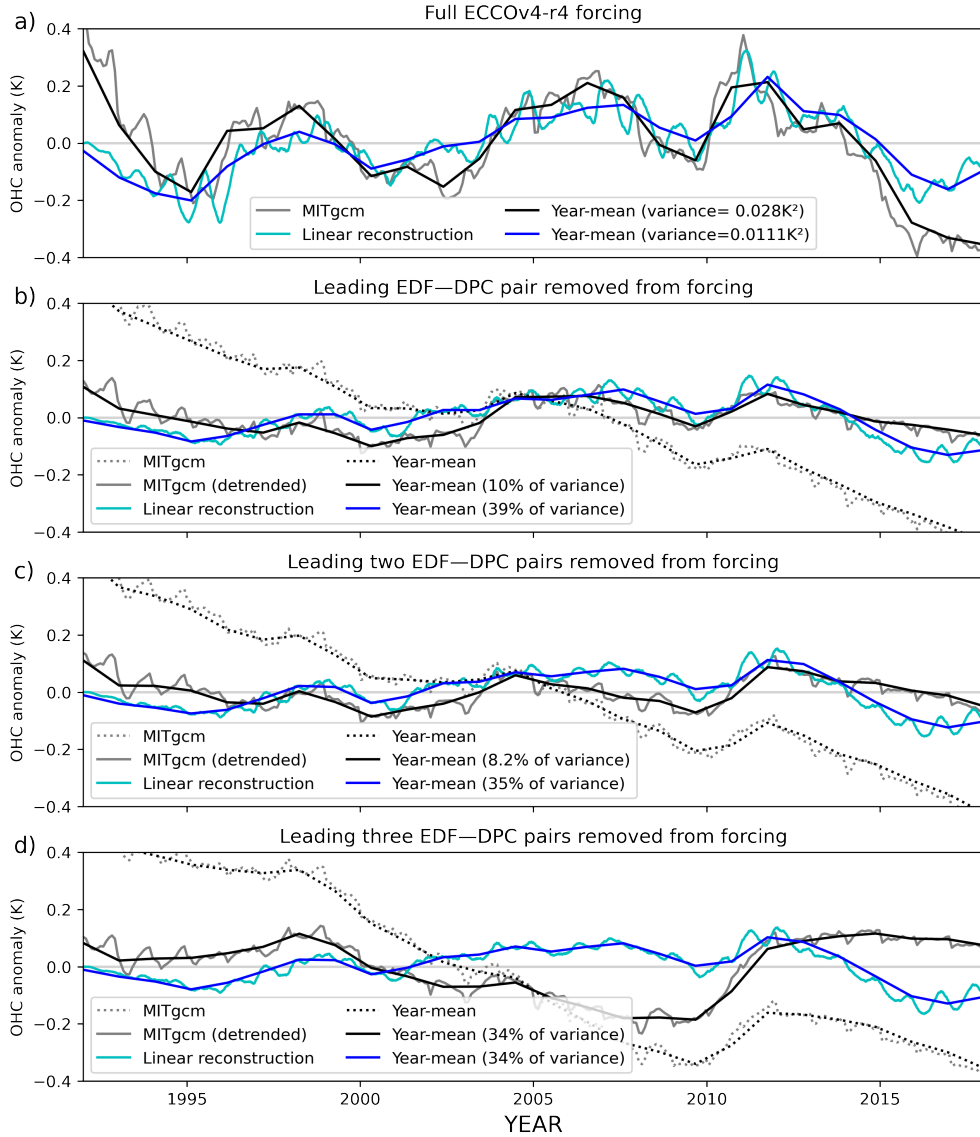
415 PCs (cf. Figure 5d and 9d), possibly owing to separability assumptions made in the derivation of
416 DPCs.

417 EDF–DPC pairs for HF (Figure 9 a-c) and WS (Figure 10 a-c) reflect a combination of influences
418 from model SOs and atmospheric flux statistics. The EDF patterns in both wind stress and heat
419 flux strongly resemble the corresponding NAO flux patterns obtained by regressing the leading
420 PC of SLP in ECCOv4-r4 onto the ECCOv4-r4 HF and WS fields (94% agreement measured by
421 pattern correlation for both HF and WS, not shown); the NAO tripole pattern (Cayan 1992a) is
422 evident in Figure 9a. While connections between EDFs, EOFs, and SOs can be complex, for heat
423 fluxes we are near one of the limit cases discussed in Section 2b whereby adjoint sensitivities can
424 be represented by a single stochastic optimal (specifically, note that the variance accounted for by
425 the leading SO in Figure 7g is a high fraction of the total). As such, the dominant EDF closely
426 resembles the pattern generated when one multiplies the leading stochastic optimal (Figure 7a) by
427 the spatial covariance of ECCOv4-r4 heat fluxes (not shown).

428 *d. Evaluating EDF–DPC patterns in the ECCOv4-r4 state estimate*

437 Next, we assess how well dominant spatial patterns derived under linearized ocean physics (from
438 the adjoint sensitivities) perform in a nonlinear ocean model constrained to fit data. The ECCO
439 state estimate is derived using a 4DVAR smoother to improve fits to observations over 1992-2017
440 (Wunsch and Heimbach 2007; Forget et al. 2015a; Fukumori et al. 2017), and the final product is
441 a forward simulation of the MITgcm under adjusted initial conditions, atmospheric conditions (or
442 fluxes), and ocean mixing parameters. We use the flux-forced version of ECCOv4-r4, which permits
443 partitioning drivers of ocean variability into respective contributions without cross terms that can
444 arise, e.g., between winds and surface air temperature when computing bulk fluxes (Fukumori et al.
445 2021).

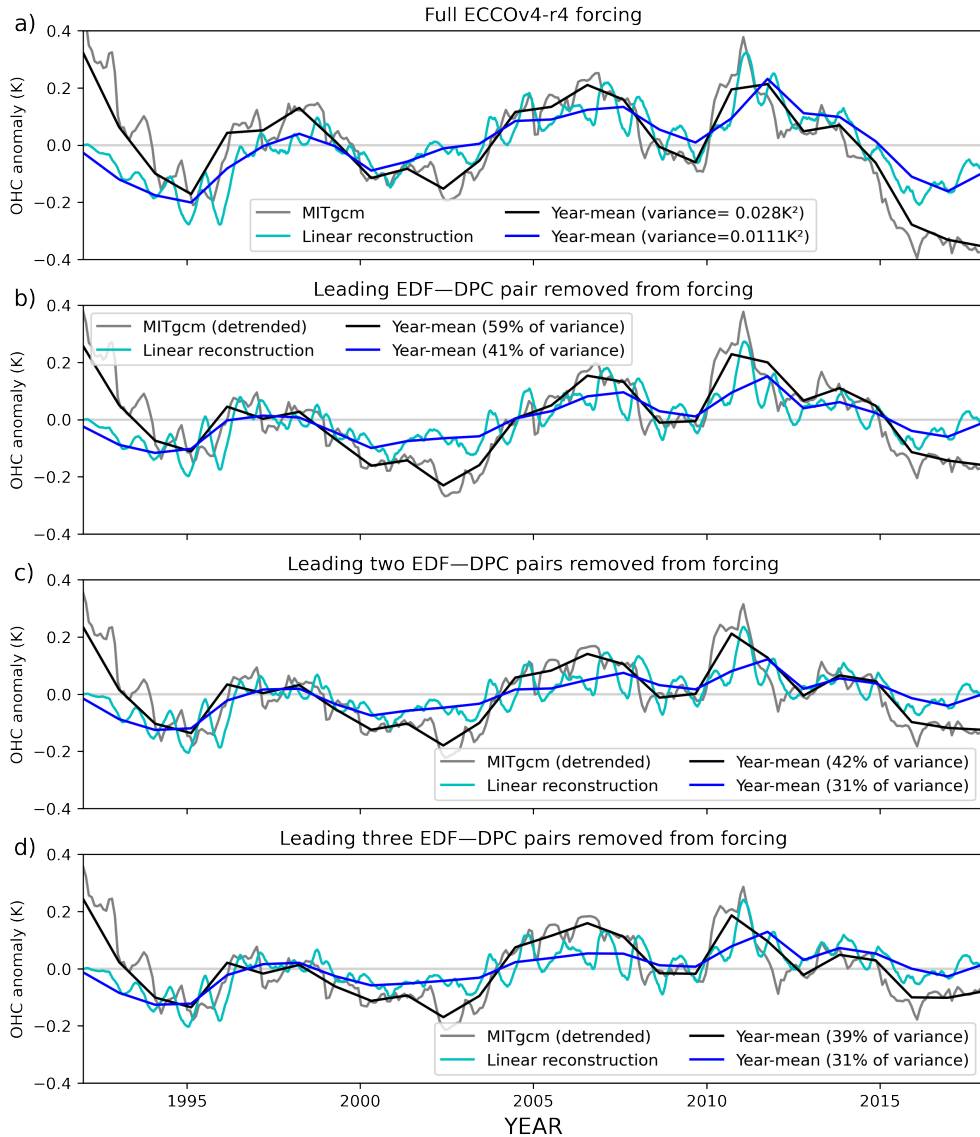
446 As an initial comparison, we convolve adjoint sensitivities with HF and WS from ECCOv4-r4
447 (Kostov et al. 2021) and find qualitative agreement with annual mean SPG HC in the ECCOv4-r4
448 state estimate (Figure 11a, duplicated in Figure 12a), suggesting that a linearized system forced
449 by HF and WS can skillfully describe historical variability in the nonlinear state estimate. Next,
450 we subtract EDF–DPC pairs from ECCOv4-r4 fluxes and use these reduced fluxes to re-compute
451 linear reconstructions and re-run the ECCOv4-r4 state estimate. Using Equation (13), we define a



429 FIG. 11. Consequences of cumulatively removing HF EDF–DPC pairs from the ECCOV4-r4 state estimate.
 430 Lines show the evolution of SPG HC over the years of the ECCOV4-r4 reconstruction under full fluxes (a) and after
 431 removing the first 1 (b), 2 (c), and 3 (d) HF EDF–DPC pairs. Black and gray lines indicate anomalies computed
 432 in the (nonlinear) MITgcm before (dotted lines) and after (solid lines) subtracting a linear trend attributed to a
 433 nonlinear response to removing HF EDF-DPC pairs. Blue lines indicate anomalies reconstructed linearly by
 434 convolving fluxes with adjoint sensitivities.

452 set of reduced fluxes by cumulatively removing the g leading EDF-DPC pairs,

$$\mathbf{U}'_g = \mathbf{U} - \sum_{k=1}^g \mathbf{p}_k \mathbf{t}_k^T. \quad (24)$$



435 FIG. 12. Same as Figure 11 but for wind stress. Panel a) is the same as Figure 11a and is presented again for
 436 comparison.

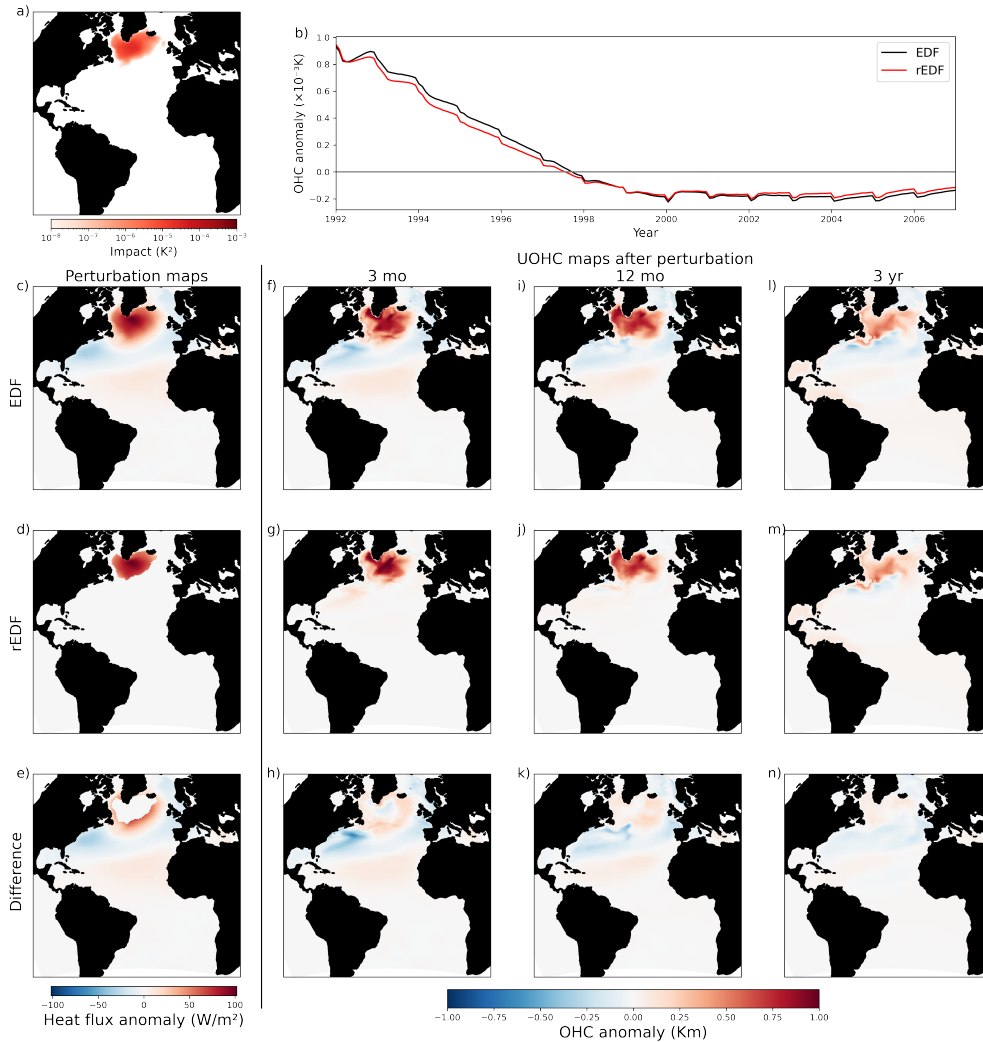
453 Removing the leading EDF-DPC pair of HF induces a downward trend in the evolution of SPG
 454 HC in the MITgcm (Figure 11b, dotted lines). The absence of this trend in the corresponding
 455 linear reconstruction (Figure 11b, blue lines) suggests that it is a nonlinear response of the model
 456 to the removal of NAO-like variability, potentially indicating a transition to a different time mean
 457 state. Such a drift could arise because the flux-forced configuration of the MITgcm does not adjust
 458 heat fluxes with changing upper-ocean temperature. Lohmann et al. (2009) also found a nonlinear

459 response of the circulation to the NAO using modified forcing experiments. While we do not
460 investigate its origins further, if we treat the drift as being a superimposed linear trend and subtract
461 it from the HC response (Figure 11b, solid gray and black lines), we find that subtraction of the
462 first HF EDF–DPC pair results in a 90% reduction in total interannual SPG HC variability in the
463 nonlinear model compared to a roughly 60% reduction in the linear reconstruction. Differences in
464 the effectiveness of the leading EDF–DPC pair in driving variability between linear and nonlinear
465 reconstructions could arise from the trend subtraction and/or additional nonlinearities. The 60%
466 variance reduction in the linear case is also less than the expected reduction of roughly 90% given
467 by σ_1^2 (far left value of left line, Figure 9g); however, some variation about σ_1^2 is expected for
468 variance reductions over finite time intervals such as the ECCOv4-r4 period. Our summary is
469 that removing the leading EDF–DPC pair results in a strong reduction in SPG HC variance in the
470 MITgcm, as also seen in the linearized system, but with an additional trend due to a nonlinear
471 HF response. Additional removal of the second EDF–DPC pair (Figure 11c) leads to a modest
472 additional reduction in QoI variance. While removal of the third pair (Figure 11d) continues to
473 reduce variance in the linear reconstruction, there is roughly a quadrupling of variance in the
474 nonlinear model relative to the case when only two EDF–DPC pairs are removed, suggesting
475 additional nonlinear responses.

476 For WS (Figure 12), removal of the leading EDF–DPC pair in the nonlinear model simulations
477 also shows qualitative agreement in variance reduction (roughly 40%) with linear reconstructions
478 (roughly 60%), and estimated σ_1^2 (roughly 70%). (Note that the variance contributions attributed
479 to WS and HF when they are removed individually can sum to more than the total variance when
480 there are covariances between those fluxes in time.) Unlike for HF, we do not observe a trend
481 or an increase in variance in the nonlinear model when subtracting one of the leading EDF–DPC
482 pairs. Similar to HF, we conclude that for this quantity of interest, the dominant mechanisms
483 identified under linear assumptions to derive EDF–DPC pairs for WS are effective in the context
484 of a nonlinear ocean GCM.

485 *e. Mechanisms leading to Subpolar Gyre heat content variability*

494 In order to evaluate the mechanisms by which leading EDFs influence the QoI, we make another
495 modification to fluxes in ECCOv4-r4. Rather than removing EDF–DPC pairs, we now add an



486 FIG. 13. Forward heat flux perturbation experiments in the MITgcm. Positive heat fluxes correspond to ocean
 487 warming. The impact map (a) illustrates the spatial distribution of HF contributions to SPG HC variability under
 488 linearized dynamics. Ranking model gridpoints by their impacts allows us to pick a subset of locations within
 489 the leading EDF (c) to constitute the leading reduced EDF (rEDF, d), eliminating features (e) that are correlated
 490 across atmospheric fluxes but have a small impact on the QoI. Panel (b) shows a high degree of similarity in SPG
 491 HC anomaly evolution when perturbed by the leading EDF and leading rEDF. Panels (f,i,l) and (g,j,m) show the
 492 evolution of upper ocean heat content anomalies in ECCOV4-r4 after initial 24-hour heat flux perturbations by
 493 EDF and rEDF on January 1992; (h,k,n) plot the difference between the two.

496 initial 24-hour perturbation of fluxes on January 1, 1992 with the spatial pattern of the leading

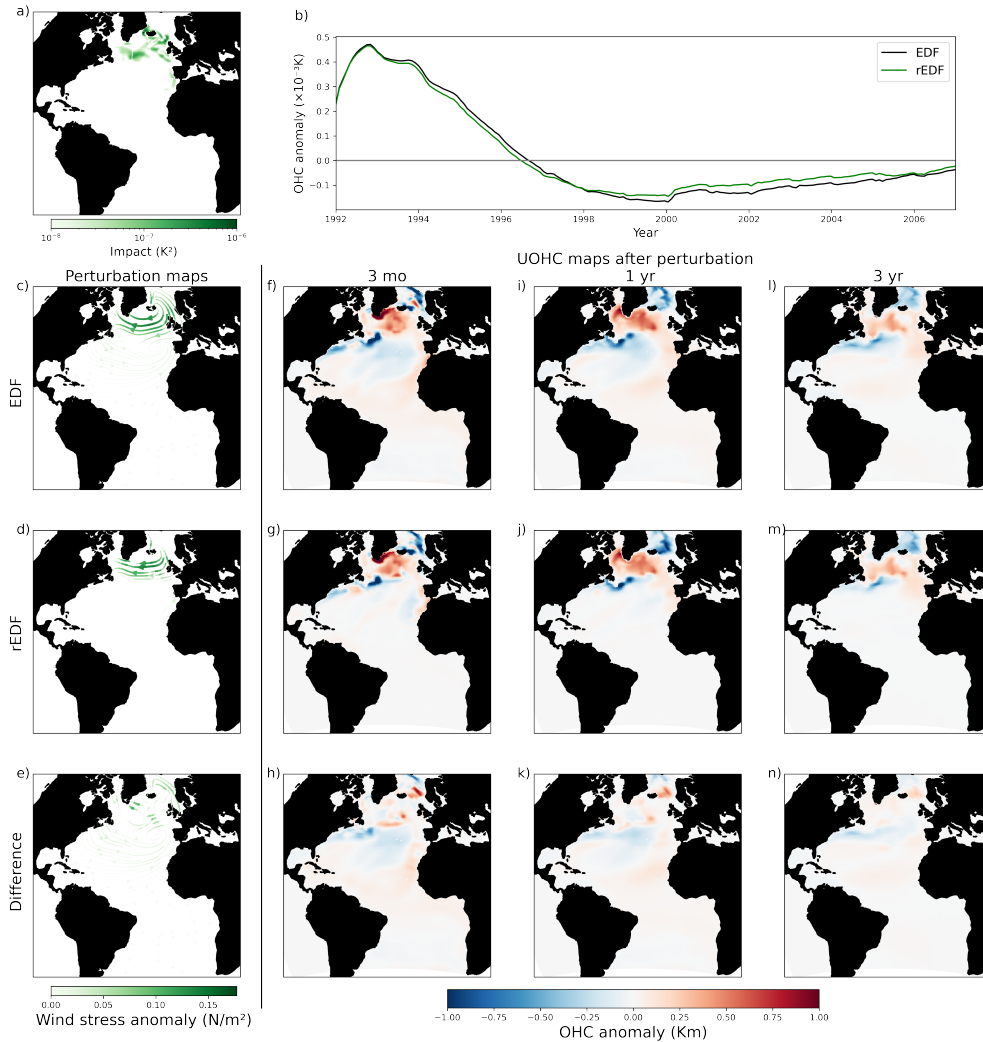


FIG. 14. Same as Figure 13 but for wind stress.

497 EDF and re-run the state estimate. Anomalies relative to the unperturbed ECCOV4-r4 show how
 498 EDF flux perturbations affect the ocean state across space and time.

499 Not all of the ocean's responses to EDF perturbations necessarily lead to QoI variance (unlike
 500 for SOs). This point is illustrated in the simple stochastic system in Section 3, in which EDFs have
 501 nonzero values at locations that do not drive QoI variability (specifically, values at locations where
 502 sensitivities are zero in the top panels in Figure 2) because fluxes at these locations are correlated
 503 with fluxes at other locations that do drive QoI variance. As such, when illustrating pathways of
 504 ocean variability, it is helpful to focus on ocean adjustments that cause QoI variance rather than
 505 those resulting merely from fluxes correlated with a QoI driver. By ranking surface grid boxes most

506 important for QoI variability using impact maps (Equation (22); Figures 13a and 14a), we define
507 rEDF (reduced EDF) patterns (Figures 13d and 14d) with smaller spatial extents that nevertheless
508 account for 99% of QoI variability. Reduced EDFs are more restricted to the SPG than full EDFs,
509 indicating that contributions within the SPG dominate HC variability there; more distant features
510 in the HF EDF are associated with the tripolar correlation fingerprint of NAO in the North Atlantic
511 (Cayan 1992b,a).

512 Evolving North Atlantic upper-ocean HC anomalies (integrated over the top 700m) in response to
513 leading EDF and rEDF perturbations illustrate the dominant pathways of fluxes en route to SPG HC
514 variability. As intended, impacts on SPG HC from EDFs and rEDFs are virtually indistinguishable
515 in time (Figures 13b and 14b), but differences between anomalous HC (panels h, k, and n) reveal
516 large-scale evolving patterns in the EDF response, particularly in the subtropical gyre, that do not
517 contribute to SPG HC variance. As such, we focus on upper-ocean heat content anomalies in
518 response to the rEDF (panels g, j, and m).

519 HC changes due to the HF rEDF perturbation are primarily confined to the SPG over a three
520 year period (Figures 13g, 13j, and 13m), with modest transport into the Labrador Sea and along
521 the tail of the Grand Banks in the Northwest Atlantic. The result (Figure 13, red line) is a warm
522 anomaly in the SPG that decays over several years with small seasonal variations, overshoots to
523 a smaller cooling anomaly, and then decays back to zero. By contrast (Figure 14, red line), SPG
524 HC in response to the WS rEDF perturbation gradually increases, peaking roughly a year after the
525 perturbation, and then (similar to the HF response) decays, overshoots, and decays back to zero.
526 Accompanying this response is cooling northeast and south of the SPG, as well as a rapid initial
527 decrease and gradual recovery in the circulation strength of the SPG (not shown). We note that
528 the WS perturbation acts to oppose time mean patterns of wind stress and wind stress curl over the
529 SPG. These results are consistent with studies attributing 1990s subpolar warming to wind stress
530 changes (Bersch 2002; Lozier et al. 2008; Sarafanov et al. 2008; Häkkinen et al. 2013) and with
531 reductions in the northward penetration of warm subtropical waters under reduced subpolar wind
532 stress curl (Häkkinen et al. 2011; Piecuch et al. 2017) that invoke changes in ocean circulation. We
533 speculate that overshoot behavior in both HF and WS responses results from changes to the density
534 structure and circulation of the SPG and surrounding waters that persist after the dissipation of
535 SPG-averaged HC anomalies, analogous to mechanisms proposed by Desbruyères et al. (2021).

536 **5. Discussion and conclusions**

537 This paper combines constraints from ocean model physics and atmospheric statistics to derive
538 the dominant atmospheric patterns and ocean pathways responsible for driving ocean variability.
539 Leading EDF-DPC pairs maximize ocean variability under assumptions of linear ocean physics and
540 space-time separability of atmosphere-ocean fluxes. These pairs are computed via a dynamics-
541 weighted principal components analysis and recover stochastic optimals and traditional EOFs
542 under limiting conditions; they can thus be seen as a hybrid of “what the ocean wants” to drive
543 variability and “what the ocean gets” from the atmosphere. As expected, these patterns outperform
544 the leading EOFs of atmospheric fluxes for driving ocean variability, even as they account for a
545 smaller fraction of the total flux variance. Applying this approach to the problem of upper-ocean
546 heat content variability in the North Atlantic subpolar gyre, we find that leading EDFs of heat
547 and momentum fluxes (Figures 9 and 10) closely resemble the North Atlantic Oscillation. By re-
548 running the ECCOV4-r4 state estimate, we show that removing leading EDF-DPC pairs is highly
549 effective at reducing SPG HC variability, though a trend in HC response may point to limitations
550 of the linear sensitivity assumption in a flux-forced model. Changes due to heat flux perturbations
551 are consistent with a primarily local, passive ocean response to stochastic variability in the gyre
552 interior, while a delay in the onset of warming due to wind stress fluxes accompanied by nonlocal
553 effects suggests an intermediate role for ocean gyre dynamics.

554 As noted in Section 1, the NAO has long been established as a source of subpolar gyre heat
555 content variability through both heat fluxes and wind stress (Böning et al. 2006; Lozier et al.
556 2008; Lohmann et al. 2009; Häkkinen et al. 2011; Zhang and Yan 2017), and our reprisal of its
557 importance may come as no surprise. Nevertheless, we argue that “rediscovering” the NAO serves
558 as a nontrivial proof of concept for the EDF–DPC approach. Just as the center of action of leading
559 EDFs was pulled to the left side of the domain in the simplified 1-D example (Figure 2), we expect
560 that the NAO-like EDF arises from a QoI that coincides geographically with the center of action
561 of the NAO, as well as one that is highly sensitive to wintertime variability. The latter constraint is
562 consistent with the definition of the NAO as the leading mode of atmospheric wintertime variability
563 (Hurrell and Deser 2009). At the same time, we caution that leading modes of sea level pressure are
564 not generally expected to be associated with leading flux EDFs for arbitrary QoIs and regions. It is
565 also instructive to contrast the leading WS EDF (Figure 10a) with the leading WS stochastic optimal

566 (Figure 8a). The absence of prominent structures along the western coast of Africa suggests that
567 while the Kelvin wave mechanism discussed by Jones et al. (2018) and Stephenson and Sévellec
568 (2021b) is a potential pathway for generating SPG HC variability, it is not a dominant mechanism
569 in practice under recent atmospheric variability.

570 The EDF-DPC approach can be extended or improved in several ways. We solved for HF
571 and WS EDFs separately and independently found strong correlations with the NAO; however,
572 future approaches could solve for multivariate EDFs across flux types. In addition, using ocean-
573 atmosphere fluxes as boundary conditions may introduce inconsistencies and drifts in perturbed
574 ECCOv4-r4 simulations due to missing turbulent flux feedbacks. An alternative could be instead to
575 compute EDFs for atmospheric variables (air temperature, winds, humidity, etc.), with the caveat
576 that there may be additional covariance relationships among these variables that need to be taken
577 into account. We have made the approximation that the sensitivity is stationary in time, meaning
578 that it depends only on the time lag τ between the QoI and fluxes; while this appears adequate
579 for our purpose, including information about time variations in sensitivities could yield additional
580 information. In this initial implementation, we defined our upper-ocean volume using a uniform
581 depth of 700 m; however, additional insights into the variability of SPG and other water masses
582 might be gained by targeting spatially varying winter mixed layer depths (Buckley et al. 2014,
583 2015) and/or a QoI defined in isopycnal coordinates. Assuming a fixed 700 m depth also neglects
584 time variations in the depth of SPG mixed layer depth, including across seasons. We hypothesize
585 that defining a QoI based on a density class would further strengthen the preference for atmospheric
586 patterns that dominate in winter time, with a qualitatively similar dominant role for the NAO.

587 By fusing information from atmospheric statistics and ocean model physics, the EDF-DPC
588 approach inherits potential sources of error from both that we have not attempted to quantify
589 here. Inferring atmospheric statistics from a finite number of samples is a well-studied problem
590 in climate variability and data assimilation (Houtekamer et al. 1998); it may be reasonable to
591 investigate a “rule of thumb” following North et al. (1982) to establish independence criteria for
592 EDFs, or to compute leading EDF-PC pairs in a subset of the time period with available flux data
593 and assess their performance over different intervals. Low-resolution ocean models also have a
594 well-documented host of shortcomings that are inherited through the adjoint sensitivities. The
595 lack of coupling and feedbacks is a limitation of the linearized, forced-ocean perspective: if an

596 atmospheric perturbation changes the ocean state in a way that in turn changes how the ocean
597 responds to future perturbations, then these effects will not be captured by linear sensitivities. The
598 importance of feedbacks might be evaluated, for instance, by applying EDF-like perturbations in a
599 coupled model.

600 While we have focused on an application for North Atlantic physical oceanography, the EDF-
601 DPC approach is generalizable to a range of applications. Within the framework of forced ocean
602 variability, we expect EDFs to be useful for any QoI whose variability is driven by atmospheric
603 fluxes. Other applications where explicitly recognizing the important role of atmospheric covari-
604 ances in determining leading drivers of ocean variability include ocean observing system design.
605 For instance, Loose et al. (2020) use adjoint sensitivities as a basis for guiding optimal observa-
606 tions of North Atlantic quantities via a “proxy potential.” The work presented here shows that
607 atmospheric conditions most likely to excite ocean stochastic optimals tend to have a large spatial
608 footprint, suggesting that proxy potential might benefit from correlations due to large-scale patterns
609 of variability. Finally, we note that a model adjoint is not required to implement an EDF-DPC
610 approach: while computational costs can be greater, ocean QoI sensitivities can also be estimated
611 via forward perturbation or “Green’s function” approaches (e.g., Menemenlis et al. 2005).

612 *Acknowledgments.* This work was supported by NASA Physical Oceanography award
613 80NSSC20K0787. We thank Ichiro Fukumori, Yavor Kostov, and Mark Cane for helpful
614 conversations. Chris Wolfe shared restart files from a long MITgcm integration. Judith Berner
615 stochastically forced the trajectory of this work by providing important insights at unpredictable
616 times. We are grateful for detailed comments from three reviewers that substantially improved the
617 paper. Supercomputing resources were provided by NASA Advanced Supercomputing and Ames
618 Research Center. The adjoint model was generated using TAF (Giering and Kaminski 1998). This
619 material is based upon work supported by the NSF National Center for Atmospheric Research,
620 which is a major facility sponsored by the U.S. National Science Foundation under Cooperative
621 Agreement No. 1852977.

622
623 Data availability statement: State estimation output used in our analyses is available from
624 the ECCO project at www.ecco-group.org/. The model configuration used for the adjoint
625 model base state is documented with necessary files at zenodo.org/record/7814839. Source

code and namelist files for flux-forced ECCOV4-r4 are located in the ECCOV4-r4 directory /MITgcm/ECCOV4/release4/flux-forced. Jupyter notebooks necessary to reproduce results from Section 3 are available at github.com/amrhein/DPCs. Python code and Jupyter notebooks demonstrating calculation of EDF-DPC pairs and other analyses performed in this paper are available at github.com/ds4g15/EDF_DPC_paper. Perturbed ECCOV4-r4 simulations generated for this paper are too large to be retained or publicly archived with available resources; documentation and methods are available from damrhein@ucar.edu.

References

- Adamjan, V. M., D. Z. Arov, and M. Kreĭn, 1971: Analytic properties of schmidt pairs for a hankel operator and the generalized schur-takagi problem. *Mathematics of the USSR-Sbornik*, **15** (1), 31.
- Adcroft, A., C. Hill, J.-M. Campin, J. Marshall, and P. Heimbach, 2004: Overview of the formulation and numerics of the {MIT GCM}. *Proceedings of the ECMWF seminar series on Numerical Methods, Recent developments in numerical methods for atmosphere and ocean modelling*, 139–149.
- Antoulas, A. C., 2005: *Approximation of large-scale dynamical systems*. SIAM.
- Barrier, N., C. Cassou, J. Deshayes, and A.-M. Treguier, 2014: Response of North Atlantic Ocean Circulation to Atmospheric Weather Regimes. *Journal of Physical Oceanography*, **44** (1), 179–201, <https://doi.org/10.1175/JPO-D-12-0217.1>, URL <http://journals.ametsoc.org/doi/abs/10.1175/JPO-D-12-0217.1><https://journals.ametsoc.org/doi/pdf/10.1175/JPO-D-12-0217.1>.
- Bersch, M., 2002: North Atlantic Oscillation–induced changes of the upper layer circulation in the northern North Atlantic Ocean. *Journal of Geophysical Research*, **107** (C10), 3156, <https://doi.org/10.1029/2001JC000901>, URL <http://doi.wiley.com/10.1029/2001JC000901>.
- Bersch, M., I. Yashayaev, and K. P. Koltermann, 2007: Recent changes of the thermohaline circulation in the subpolar North Atlantic. *Ocean Dynamics*, **57** (3), 223–235, <https://doi.org/10.1007/s10236-007-0104-7>, arXiv:1011.1669v3.
- Böning, C. W., M. Scheinert, J. Dengg, A. Biastoch, and A. Funk, 2006: Decadal variability of subpolar gyre transport and its reverberation in the North Atlantic overturning. *Geophysical*

654 *Research Letters*, **33** (21), L21S01, <https://doi.org/10.1029/2006GL026906>, URL <http://doi.wiley.com/10.1029/2006GL026906>.

655

656 Brunton, S. L., and J. N. Kutz, 2022: *Data-driven science and engineering: Machine learning, dynamical systems, and control*. Cambridge University Press.

657

658 Buckley, M. W., R. M. Ponte, G. Forget, and P. Heimbach, 2014: Low-frequency SST and upper-ocean heat content variability in the North Atlantic. *Journal of Climate*, **27** (13), 4996–5018, <https://doi.org/10.1175/JCLI-D-13-00316.1>.

659

660

661 Buckley, M. W., R. M. Ponte, G. Forget, and P. Heimbach, 2015: Determining the origins of advective heat transport convergence variability in the north atlantic. *Journal of Climate*, **28** (10), 3943–3956.

662

663

664 Bugnion, V., C. Hill, and P. H. Stone, 2006a: An Adjoint Analysis of the Meridional Overturning Circulation in a Hybrid Coupled Model. *Journal of Climate*, **19** (15), 3751–3767, <https://doi.org/10.1175/JCLI3821.1>, URL <http://journals.ametsoc.org/doi/abs/10.1175/JCLI3821.1>.

665

666

667 Bugnion, V., C. Hill, and P. H. Stone, 2006b: An Adjoint Analysis of the Meridional Overturning Circulation in an Ocean Model. *Journal of Climate*, **19** (15), 3732–3750, <https://doi.org/10.1175/JCLI3787.1>, URL <http://journals.ametsoc.org/doi/abs/10.1175/JCLI3787.1>.

668

669

670 Cayan, D. R., 1992a: Latent and sensible heat flux anomalies over the northern oceans: Driving the sea surface temperature. *Journal of Physical Oceanography*, **22** (8), 859–881.

671

672 Cayan, D. R., 1992b: Latent and sensible heat flux anomalies over the northern oceans: The connection to monthly atmospheric circulation. *Journal of climate*, **5** (4), 354–369.

673

674 Chen, W., M. G. Genton, and Y. Sun, 2021: Space-time covariance structures and models. *Annual Review of Statistics and Its Application*, **8**, 191–215.

675

676 Chhak, K. C., and A. M. Moore, 2007: The North Atlantic Oscillation as a source of stochastic forcing of the wind-driven ocean circulation. *Dynamics of atmospheres and oceans*, **43** (3-4), 151–170.

677

678

679 Chhak, K. C., A. M. Moore, and R. F. Milliff, 2009: Stochastic forcing of ocean variability by the north atlantic oscillation. *Journal of physical oceanography*, **39** (1), 162–184.

680

- 681 Czeschel, L., C. Eden, and R. J. Greatbatch, 2012: On the Driving Mechanism of the An-
682 nual Cycle of the Florida Current Transport. *Journal of Physical Oceanography*, **42** (5),
683 824–839, <https://doi.org/10.1175/JPO-D-11-0109.1>, URL [http://journals.ametsoc.org/doi/abs/](http://journals.ametsoc.org/doi/abs/10.1175/JPO-D-11-0109.1)
684 [10.1175/JPO-D-11-0109.1](http://journals.ametsoc.org/doi/abs/10.1175/JPO-D-11-0109.1).
- 685 Czeschel, L., D. P. Marshall, and H. L. Johnson, 2010: Oscillatory sensitivity of Atlantic overturn-
686 ing to high-latitude forcing. *Geophysical Research Letters*, **37** (10), n/a–n/a, [https://doi.org/10.](https://doi.org/10.1029/2010GL043177)
687 [1029/2010GL043177](https://doi.org/10.1029/2010GL043177), URL <http://doi.wiley.com/10.1029/2010GL043177>, [10/2010GL043177](http://doi.wiley.com/10.1029/2010GL043177).
- 688 Desbruyères, D., L. Chafik, and G. Maze, 2021: A shift in the ocean circulation has warmed the
689 subpolar north atlantic ocean since 2016. *Communications Earth & Environment*, **2** (1), 48.
- 690 Deser, C., M. A. Alexander, S.-P. Xie, and A. S. Phillips, 2010: Sea surface temperature variability:
691 Patterns and mechanisms. *Annual review of marine science*, **2**, 115–143.
- 692 Farrell, B. F., and P. J. Ioannou, 1996: Generalized stability theory. part i: Autonomous operators.
693 *Journal of Atmospheric Sciences*, **53** (14), 2025–2040.
- 694 Farrell, B. F., and P. J. Ioannou, 2001: Accurate low-dimensional approximation of the linear
695 dynamics of fluid flow. *Journal of the atmospheric sciences*, **58** (18), 2771–2789.
- 696 Forget, G., J.-M. Campin, P. Heimbach, C. N. Hill, R. M. Ponte, and C. Wunsch, 2015a: {ECCO}
697 version 4: an integrated framework for non-linear inverse modeling and global ocean state
698 estimation.
- 699 Forget, G., D. Ferreira, and X. Liang, 2015b: On the observability of turbulent transport rates
700 by Argo: Supporting evidence from an inversion experiment. *Ocean Science*, **11** (5), 839–853,
701 <https://doi.org/10.5194/os-11-839-2015>.
- 702 Foukal, N. P., and M. S. Lozier, 2017: Assessing variability in the size and strength of the
703 North Atlantic subpolar gyre. *Journal of Geophysical Research: Oceans*, **122** (8), 6295–6308,
704 <https://doi.org/10.1002/2017JC012798>, URL <http://doi.wiley.com/10.1002/2017JC012798>.
- 705 Frajka-Williams, E., C. Beaulieu, and A. Ducez, 2017: Emerging negative Atlantic Multidecadal
706 Oscillation index in spite of warm subtropics. *Scientific Reports*, **7** (1), 1–8, [https://doi.org/](https://doi.org/10.1038/s41598-017-11046-x)
707 [10.1038/s41598-017-11046-x](https://doi.org/10.1038/s41598-017-11046-x), URL <http://dx.doi.org/10.1038/s41598-017-11046-x>.

- 708 Frankignoul, C., and K. Hasselmann, 1977: {S}tochastic climate models, part {II} application to
709 sea-surface temperature anomalies and thermocline variability. *Tellus*, **29** (4), 289–305.
- 710 Fukumori, I., P. Heimbach, R. M. Ponte, C. Wunsch, I. Fukumori, P. Heimbach, R. M. Ponte,
711 and C. Wunsch, 2018: A Dynamically Consistent, Multi-Variable Ocean Climatology. *Bul-*
712 *letin of the American Meteorological Society*, BAMS–D–17–0213.1, [https://doi.org/10.1175/](https://doi.org/10.1175/BAMS-D-17-0213.1)
713 BAMS-D-17-0213.1, URL <http://journals.ametsoc.org/doi/10.1175/BAMS-D-17-0213.1>.
- 714 Fukumori, I., O. Wang, and I. Fenty, 2021: Causal mechanisms of sea level and freshwater content
715 change in the beaufort sea. *Journal of Physical Oceanography*, **51** (10), 3217–3234.
- 716 Fukumori, I., O. Wang, I. Fenty, G. Forget, P. Heimbach, and R. M. Ponte, 2017: ECCO Version
717 4 Release 3. Tech. rep. URL <https://dspace.mit.edu/handle/1721.1/110380>.
- 718 Fukumori, I., O. Wang, W. Llovel, I. Fenty, and G. Forget, 2015: A near-uniform fluctu-
719 ation of ocean bottom pressure and sea level across the deep ocean basins of the Arctic
720 Ocean and the Nordic Seas. *Progress in Oceanography*, **134**, 152–172, [https://doi.org/10.1016/](https://doi.org/10.1016/j.pocean.2015.01.013)
721 [j.pocean.2015.01.013](http://dx.doi.org/10.1016/j.pocean.2015.01.013), URL <http://dx.doi.org/10.1016/j.pocean.2015.01.013><http://linkinghub.elsevier.com/retrieve/pii/S0079661115000245>.
- 722
- 723 Giering, R., and T. Kaminski, 1998: {R}ecipes for adjoint code construction. *ACM Transactions*
724 *on Mathematical Software (TOMS)*, **24** (4), 437–474.
- 725 Häkkinen, S., P. B. Rhines, and D. L. Worthen, 2011: Warm and saline events embedded in
726 the meridional circulation of the northern North Atlantic. *Journal of Geophysical Research:*
727 *Oceans*, **116** (C3).
- 728 Häkkinen, S., P. B. Rhines, and D. L. Worthen, 2013: Northern north atlantic sea surface height and
729 ocean heat content variability. *Journal of Geophysical Research: Oceans*, **118** (7), 3670–3678.
- 730 Hasselmann, K., 1976: {S}tochastic climate models part {I}. {T}heory. *Tellus*, **28** (6), 473–485.
- 731 Hasselmann, K., 1993: Optimal fingerprints for the detection of time-dependent climate change.
732 *Journal of Climate*, **6** (10), 1957–1971.
- 733 Houtekamer, P. L., H. L. Mitchell, P. L. Houtekamer, and H. L. Mitchell, 1998:
734 Data Assimilation Using an Ensemble Kalman Filter Technique. *Monthly Weather Re-*

735 view, **126 (3)**, 796–811, [https://doi.org/10.1175/1520-0493\(1998\)126<0796:DAUAEK>2.0.CO;](https://doi.org/10.1175/1520-0493(1998)126<0796:DAUAEK>2.0.CO;2)
736 2, URL [http://journals.ametsoc.org/doi/abs/10.1175/1520-0493{\%}281998{\%}29126{\%}](http://journals.ametsoc.org/doi/abs/10.1175/1520-0493{\%}281998{\%}29126{\%}3C0796{\%}3ADAUAEK{\%}3E2.0.CO{\%}3B2)
737 [}3C0796{\%}3ADAUAEK{\%}3E2.0.CO{\%}3B2](http://journals.ametsoc.org/doi/abs/10.1175/1520-0493{\%}281998{\%}29126{\%}3C0796{\%}3ADAUAEK{\%}3E2.0.CO{\%}3B2).

738 Hurrell, J. W., and C. Deser, 2009: North Atlantic climate variability: The role of the North Atlantic
739 Oscillation. *Journal of Marine Systems*, **78 (1)**, 28–41, [https://doi.org/10.1016/j.jmarsys.2008.](https://doi.org/10.1016/j.jmarsys.2008.11.026)
740 [11.026](https://doi.org/10.1016/j.jmarsys.2008.11.026), URL <http://linkinghub.elsevier.com/retrieve/pii/S0924796309000815>.

741 Jones, D., G. Forget, B. Sinha, S. Josey, E. Boland, A. Meijers, and E. Shuckburgh, 2018: Local
742 and Remote Influences on the Heat Content of the Labrador Sea: an Adjoint Sensitivity Study.
743 *Journal of Geophysical Research: Oceans*, 1–22, <https://doi.org/10.17605/OSF.IO/KC2U9>,
744 URL <https://eartharxiv.org/kc2u9/>.

745 Kim, W. M., S. Yeager, P. Chang, and G. Danabasoglu, 2016: Atmospheric conditions associated
746 with Labrador Sea deep convection: New insights from a case study of the 2006/07 and 2007/08
747 winters. *Journal of Climate*, **29 (14)**, 5281–5297, <https://doi.org/10.1175/JCLI-D-15-0527.1>.

748 Kleeman, R., 2008: Stochastic theories for the irregularity of enso. *Philosophical Transactions of*
749 *the Royal Society A: Mathematical, Physical and Engineering Sciences*, **366 (1875)**, 2509–2524.

750 Kleeman, R., and A. M. Moore, 1997: A theory for the limitation of enso predictability due to
751 stochastic atmospheric transients. *Journal of the atmospheric sciences*, **54 (6)**, 753–767.

752 Köhl, A., and D. Stammer, 2004: Optimal Observations for Variational Data Assimilation.
753 *Journal of Physical Oceanography*, **34 (3)**, 529–542, <https://doi.org/10.1175/2513.1>, URL
754 <http://journals.ametsoc.org/doi/abs/10.1175/2513.1>.

755 Kostov, Y., H. L. Johnson, and D. P. Marshall, 2019: AMOC sensitivity to surface buoyancy
756 fluxes : the role of air - sea feedback mechanisms. *Climate Dynamics*, **1 (2014)**, [https://doi.org/](https://doi.org/10.1007/s00382-019-04802-4)
757 [10.1007/s00382-019-04802-4](https://doi.org/10.1007/s00382-019-04802-4), URL <https://doi.org/10.1007/s00382-019-04802-4>.

758 Kostov, Y., M.-J. Messias, H. Mercier, H. L. Johnson, and D. P. Marshall, 2022: Fast mechanisms
759 linking the labrador sea with subtropical atlantic overturning. *Climate Dynamics*, 1–26.

760 Kostov, Y., and Coauthors, 2021: Distinct sources of interannual subtropical and subpolar atlantic
761 overturning variability. *Nature Geoscience*, **14 (7)**, 491–495.

762 Kushnir, Y., W. Robinson, I. Bladé, N. Hall, S. Peng, and R. Sutton, 2002: Atmospheric gm
763 response to extratropical sst anomalies: Synthesis and evaluation. *Journal of Climate*, **15** (16),
764 2233–2256.

765 Large, W. G., and S. G. Yeager, 2004: *{D}iurnal to decadal global forcing for ocean and sea-ice*
766 *models: the data sets and flux climatologies*. National Center for Atmospheric Research Boulder.

767 Lohmann, K., H. Drange, and M. Bentsen, 2009: Response of the North Atlantic subpolar gyre to
768 persistent North Atlantic oscillation like forcing. *Climate dynamics*, **32** (2), 273–285.

769 Loose, N., P. Heimbach, H. Pillar, and K. H. Nisancioglu, 2020: Quantifying dynamical proxy po-
770 tential through shared adjustment physics in the north atlantic. *Journal of Geophysical Research:*
771 *Oceans*, **125** (9), e2020JC016 112.

772 Lorenz, E. N., 1956: *Empirical orthogonal functions and statistical weather prediction*, Vol. 1.
773 Massachusetts Institute of Technology, Department of Meteorology Cambridge.

774 Lozier, M. S., S. Leadbetter, R. G. Williams, V. Roussenov, M. S. C. Reed, and N. J. Moore, 2008:
775 The Spatial Pattern and Mechanisms of Heat-Content Change in the North Atlantic. *Science*,
776 **319** (5864), 800–803, <https://doi.org/10.1126/science.1146436>, URL <http://www.sciencemag.org/cgi/doi/10.1126/science.1146436>, arXiv:1011.1669v3.

778 MacGilchrist, G. A., H. L. Johnson, C. Lique, and D. P. Marshall, 2021: Demons in the
779 north atlantic: Variability of deep ocean ventilation. *Geophysical Research Letters*, **48** (9),
780 e2020GL092 340.

781 Marotzke, J., R. Giering, K. Q. Zhang, D. Stammer, C. Hill, and T. Lee, 1999: Construction of the
782 adjoint mit ocean general circulation model and application to atlantic heat transport sensitivity.
783 *Journal of Geophysical Research: Oceans*, **104** (C12), 29 529–29 547.

784 Marshall, J., A. Adcroft, C. Hill, L. Perelman, and C. Heisey, 1997: *{A}* finite-volume, incom-
785 pressible *{N}*avier *{S}*tokes model for studies of the ocean on parallel computers. *Journal of*
786 *Geophysical Research: Oceans (1978–2012)*, **102** (C3), 5753–5766.

787 Marshall, J., and Coauthors, 2001: North atlantic climate variability: phenomena, impacts and
788 mechanisms. *International Journal of Climatology: A Journal of the Royal Meteorological*
789 *Society*, **21** (15), 1863–1898.

- 790 Mazloff, M. R., 2012: On the sensitivity of the drake passage transport to air-sea momentum flux.
791 *Journal of Climate*, **25** (7), 2279–2290, <https://doi.org/10.1175/JCLI-D-11-00030.1>.
- 792 Menemenlis, D., I. Fukumori, and T. Lee, 2005: Using green's functions to calibrate an ocean
793 general circulation model. *Monthly weather review*, **133** (5), 1224–1240.
- 794 Moore, A. M., H. G. Arango, E. Di Lorenzo, B. D. Cornuelle, A. J. Miller, and D. J. Neilson, 2004:
795 A comprehensive ocean prediction and analysis system based on the tangent linear and adjoint
796 of a regional ocean model. *Ocean Modelling*, **7** (1-2), 227–258.
- 797 Moore, A. M., J. Fiechter, and C. A. Edwards, 2022: A linear stochastic emulator of the california
798 current system using balanced truncation. *Ocean Modelling*, **174**, 102 023.
- 799 Moore, A. M., and R. Kleeman, 1999: Stochastic forcing of enso by the intraseasonal oscillation.
800 *Journal of Climate*, **12** (5), 1199–1220.
- 801 Moore, A. M., and Coauthors, 2006: Optimal forcing patterns for coupled models of enso. *Journal*
802 *of climate*, **19** (18), 4683–4699.
- 803 Moore, B., 1981: Principal component analysis in linear systems: Controllability, observability,
804 and model reduction. *IEEE transactions on automatic control*, **26** (1), 17–32.
- 805 North, G. R., T. L. Bell, and R. F. Cahalan, 1982: Sampling Errors in the Estimation of Empirical Or-
806 thogonal Funtions. URL [http://journals.ametsoc.org/doi/abs/10.1175/1520-0493\(1982\)110{\%
807 }3C0699:SEITEO{\%3E2.0.CO;2, 699–706 pp., https://doi.org/10.1175/1520-0493\(1982\)
808 110\(0699:SEITEO\)2.0.CO;2](http://journals.ametsoc.org/doi/abs/10.1175/1520-0493(1982)110{\%3C0699:SEITEO{\%3E2.0.CO;2, 699–706 pp., https://doi.org/10.1175/1520-0493(1982)110(0699:SEITEO)2.0.CO;2).
- 809 Oldenburg, D., R. C. Wills, K. C. Armour, L. Thompson, and L. C. Jackson, 2021: Mechanisms of
810 low-frequency variability in north atlantic ocean heat transport and amoc. *Journal of Climate*,
811 **34** (12), 4733–4755.
- 812 Ortega, P., J. Robson, R. T. Sutton, and M. B. Andrews, 2017: Mechanisms of decadal variability
813 in the labrador sea and the wider north atlantic in a high-resolution climate model. *Climate*
814 *Dynamics*, **49**, 2625–2647.
- 815 Piecuch, C. G., R. M. Ponte, C. M. Little, M. W. Buckley, and I. Fukumori, 2017: Mechanisms
816 underlying recent decadal changes in subpolar North Atlantic Ocean heat content. *Journal of Geo-*

817 *physical Research: Oceans*, **122 (9)**, 7181–7197, <https://doi.org/10.1002/2017JC012845>, URL
818 <http://doi.wiley.com/10.1002/2016JC012264><http://doi.wiley.com/10.1002/2017JC012845>.

819 Pillar, H. R., P. Heimbach, H. L. Johnson, and D. P. Marshall, 2016: Dynamical Attribution
820 of Recent Variability in Atlantic Overturning. *Journal of Climate*, **29 (9)**, 3339–3352,
821 <https://doi.org/10.1175/JCLI-D-15-0727.1>, URL <https://journals.ametsoc.org/doi/pdf/10.1175/JCLI-D-15-0727.1>
822 <http://journals.ametsoc.org/doi/10.1175/JCLI-D-15-0727.1>.

823 Rowley, C. W., 2005: Model reduction for fluids, using balanced proper orthogonal decomposition.
824 *International Journal of Bifurcation and Chaos*, **15 (03)**, 997–1013.

825 Sarafanov, A., A. Falina, A. Sokov, and A. Demidov, 2008: Intense warming and salinification
826 of intermediate waters of southern origin in the eastern subpolar north atlantic in the 1990s to
827 mid-2000s. *Journal of Geophysical Research: Oceans*, **113 (C12)**.

828 Stephenson, D., and F. Sévellec, 2021a: The active and passive roles of the ocean in generating
829 basin-scale heat content variability. *Geophysical Research Letters*, **48 (19)**, e2020GL091874.

830 Stephenson, D., and F. Sévellec, 2021b: Dynamical attribution of north atlantic interdecadal
831 predictability to oceanic and atmospheric turbulence under diagnosed and optimal stochastic
832 forcing. *Journal of Climate*, **34 (22)**, 9153–9179.

833 Stommel, H., 1979: {D}etermination of water mass properties of water pumped down from the
834 {E}kman layer to the geostrophic flow below. *Proceedings of the National Academy of Sciences*,
835 **76 (7)**, 3051–3055.

836 Tesdal, J.-E., R. P. Abernathy, J. I. Goes, A. L. Gordon, and T. W. N. Haine, 2018: Salinity
837 Trends within the Upper Layers of the Subpolar North Atlantic. *Journal of Climate*, **31 (7)**,
838 2675–2698, <https://doi.org/10.1175/JCLI-D-17-0532.1>, URL <http://journals.ametsoc.org/doi/10.1175/JCLI-D-17-0532.1>.
839

840 Vidard, A., P.-A. Bouttier, and F. Vigilant, 2015: NemoTam: tangent and adjoint models for the
841 ocean modelling platform nemo. *Geoscientific Model Development*, **8 (4)**, 1245–1257.

842 Wills, R. C., K. C. Armour, D. S. Battisti, and D. L. Hartmann, 2019: Ocean–atmosphere
843 dynamical coupling fundamental to the atlantic multidecadal oscillation. *Journal of Climate*,
844 **32 (1)**, 251–272.

- 845 Wolfe, C. L., P. Cessi, and B. D. Cornuelle, 2017: An intrinsic mode of interannual variability in
846 the indian ocean. *Journal of Physical Oceanography*, **47** (3), 701–719.
- 847 Wunsch, C., and P. Heimbach, 2007: {P}ractical global oceanic state estimation. *Physica D:
848 Nonlinear Phenomena*, **230** (1), 197–208, <https://doi.org/10.1016/j.physd.2006.09.040>.
- 849 Xu, T., M. Newman, M. A. Alexander, and A. Capotondi, 2024: A forecast test for reducing
850 dynamical dimensionality of model emulators. *Journal of Advances in Modeling Earth Systems*,
851 **16** (1).
- 852 Yeager, S., and Coauthors, 2021: An outsized role for the labrador sea in the multidecadal variability
853 of the atlantic overturning circulation. *Science Advances*, **7** (41), eabh3592.
- 854 Zanna, L., and E. Tziperman, 2008: Optimal surface excitation of the thermohaline circulation.
855 *Journal of Physical Oceanography*, **38** (8), 1820–1830.
- 856 Zavala-Garay, J., A. Moore, C. Perez, and R. Kleeman, 2003: The response of a coupled model of
857 enso to observed estimates of stochastic forcing. *Journal of Climate*, **16** (17), 2827–2842.
- 858 Zhang, W., and X.-H. Yan, 2017: The subpolar north atlantic ocean heat content variability and its
859 decomposition. *Scientific Reports*, **7** (1), 1–8.